

# High-Resolution Spatial and Temporal Analysis of the Aftershock Sequence of the 23 August 2011 Mw 5.8 Mineral, Virginia, Earthquake

Author: Stephen Glenn Hilfiker

Persistent link: <http://hdl.handle.net/2345/bc-ir:107179>

This work is posted on [eScholarship@BC](#),  
Boston College University Libraries.

---

Boston College Electronic Thesis or Dissertation, 2016

Copyright is held by the author. This work is licensed under a Creative Commons Attribution-NonCommercial-NoDerivatives 4.0 International License (<http://creativecommons.org/licenses/by-nc-nd/4.0>).

Boston College

The Graduate School of Arts and Sciences

Department of Earth and Environmental Sciences

HIGH-RESOLUTION SPATIAL AND TEMPORAL ANALYSIS OF THE  
AFTERSHOCK SEQUENCE OF THE 23 AUGUST 2011 Mw 5.8 MINERAL,  
VIRGINIA, EARTHQUAKE

a thesis

by

STEPHEN GLENN HILFIKER

submitted in partial fulfillment of the requirements

for the degree of

Master of Science

August 2016



## **High-Resolution Spatial and Temporal Analysis of the Aftershock Sequence of the 23 August 2011 Mw 5.8 Mineral, Virginia, Earthquake**

Stephen G. Hilfiker  
John E. Ebel

### **ABSTRACT**

Studies of aftershock sequences in the Central Virginia Seismic Zone (CVSZ) provide critical details of the subsurface geologic structures responsible for past and (possibly) future earthquakes in an intraplate setting. The 23 August 2011  $M_w$  5.8 Mineral, Virginia, earthquake, the largest magnitude event recorded in the CVSZ, caused widespread damage and generated a lengthy and well-recorded aftershock sequence. Over 1600 aftershocks were recorded using a dense network of seismometers in the four months following the mainshock, offering the unique opportunity to study the fault structure responsible for the post-main event seismicity. Previous work has not accurately determined the geometry of the fault structure or the migration of post-mainshock seismicity and association of the 2011 event with a known fault has been unsuccessful. In this study, relative locations of recorded aftershocks were calculated using a version of the double-difference location method outlined in Ebel et al. (2008) to generate an accurate model of the fault structure. The moment tensor inversion technique of Ebel and Bonjer (1990) was used to generate focal mechanisms of dozens of the aftershocks at various locations on the fault structure. Results from the double-difference and moment tensor inversion methods were used to map the structure responsible for the aftershock sequence in high resolution. The calculated fault structure has planes with similar strikes and dips as known faults and geologic structures in the CVSZ. In-depth analysis of this aftershock sequence provides seismologists with the opportunity to better understand the seismic hazards present in poorly understood intraplate seismic zones.

# TABLE OF CONTENTS

	Page
TABLE OF CONTENTS.....	i
ACKNOWLEDGEMENTS.....	ii
INTRODUCTION.....	1
BACKGROUND.....	3
<u>Geologic Setting</u> .....	3
<u>Past Work</u> .....	9
METHODS.....	12
<u>Relative Locations</u> .....	12
<u>Moment Tensor Inversion</u> .....	22
DISCUSSION.....	29
CONCLUSION.....	36
REFERENCES.....	38

## ACKNOWLEDGEMENTS

Thank you to Qimin Wu and Martin Chapman at the Virginia Tech Seismological Observatory for providing the absolute aftershock locations used in this study. Thank you to Dr. John E. Ebel for his endless patience, wisdom, and advice. Thank you to my thesis committee for their thoughtful comments and advice. Thank you to the Boston College Department of Earth and Environmental Sciences and Weston Observatory. This work was supported in part by the United States Geological Survey (USGS) under USGS award numbers G13AP00044 and G13AP00043. The views and conclusions contained in this document are that of the author and do not necessarily represent opinions of the government.

## INTRODUCTION

Large and damaging earthquakes in the densely populated eastern United States are difficult to forecast due to the long recurrence intervals between events and the lack of an active plate boundary along which earthquakes typically occur. The  $M_w$  5.8 Mineral, Virginia, earthquake of 23 August 2011 is one of the largest seismic events known to have occurred east of the Rocky Mountains in historic times, and the largest known earthquake in the Central Virginia Seismic Zone (CVSZ). The earthquake caused significant structural damage in Washington, D.C. and prompted a temporary shutdown of the North Anna Nuclear Power Plant, located only 22 km from the epicenter (Figure 1). Many mapped faults exist in the CVSZ, but the Mineral, Virginia, earthquake has not been associated with a known fault (Wolin et al., 2012; Chapman, 2013; Figure 1). Previous studies have determined the regional crustal structure, fault locations, and geologic history of the CVSZ (James et al., 1968; Hopper and Bollinger, 1971; Bollinger and Hopper, 1972; Bollinger, 1973a, 1973b; Bollinger and Sibol, 1985; Coruh et al., 1988; Pratt et al., 1988; Stein et al., 1989; Fail, 1998; Withjack et al., 1998; Bailey, 1999a; Kim and Chapman, 2005) while others have attempted to attribute the Mineral, Virginia earthquake to a known or new fault (Herrmann, 2011; Horton et al., 2012a; Horton et al., 2012b; Chapman, 2013; Burton et al., 2014; McNamara et al., 2014a; McNamara et al., 2014b; Burton et al., 2015; Horton et al., 2015a; Horton et al., 2015b; Hughes et al., 2015; Pratt et al., 2015; Shah et al., 2015).

GENERALIZED GEOLOGIC MAP OF THE CENTRAL VIRGINIA PIEDMONT  
WITH FAULTS AND EARTHQUAKES (M>2, 1973-2011)

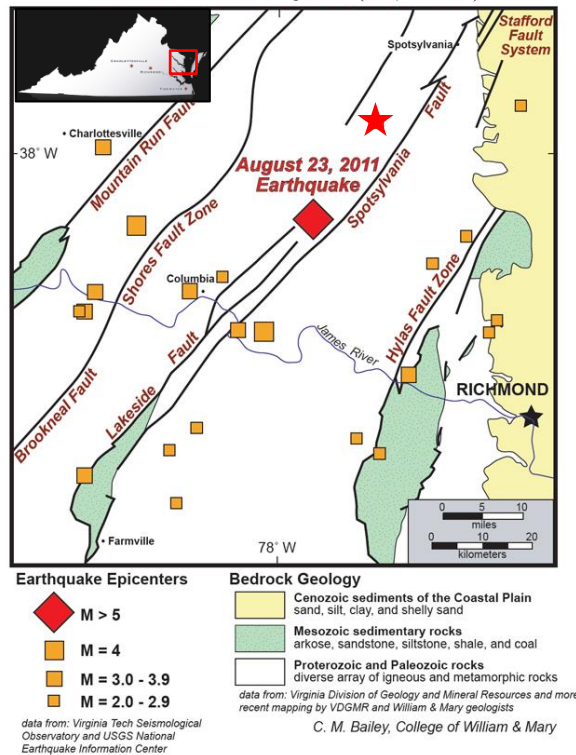


**Figure 1:** Map showing known fault locations, geology, and the epicenter of the 23 August 2011 Mineral, Virginia, earthquake. The red star is the approximate location of the North Anna Nuclear Power Plant. The  $M_w$  5.8 earthquake has not been closely associated with any previously mapped faults (Graizer et al., 2013).

Two separate analysis methods are used in this study in an effort to calculate the geometry of the fault structures illuminated by the aftershocks in high resolution, determine post-mainshock fault motion, and to discover temporal patterns in the migration of aftershock seismicity along the fault structure. The first analysis method used in this study, from Ebel et al. (2008), is a modified version of the double-difference earthquake location scheme of Waldhauser and Ellsworth (2000) and is used to calculate precise relative aftershock locations. The second analysis method is the moment tensor inversion technique of Ebel and Bonjer (1990), which is used to calculate focal mechanisms for aftershocks on the fault structure. The calculated geometry of the fault structure is compared with known faults and pre-existing planes of weakness near the

location of the projected intersection of the fault structure with Earth's surface to determine if the fault structure activated by the 23 August, 2011 main event can be found.

## BACKGROUND

### Geologic Setting

The CVSZ is a 120 by 150 km (N-S by E-W) seismic zone in the eastern United States stretching from Richmond, VA to Lynchburg, VA (Bollinger and Sibol, 1985). Reports of earthquakes felt in the CVSZ extend as far back as 1774. Studies using accounts from newspapers, letters, and diaries have discerned 84 earthquakes in the subsequent 203 years, leading to the naming of this region as the CVSZ (Hopper and Bollinger, 1971; Bollinger and Hopper; 1972; Bollinger, 1973a, 1973b).

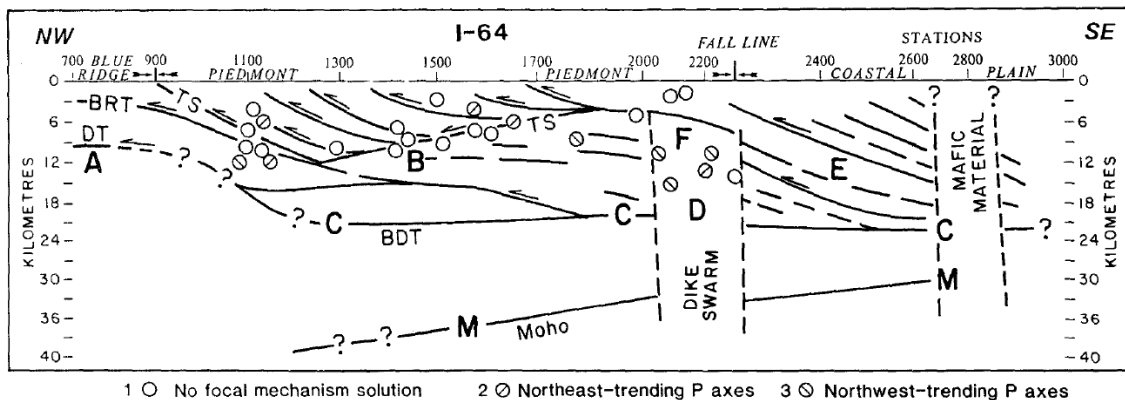


**Figure 2:** Simplified cross-section from Charlottesville to Richmond, VA along Interstate 64 (I-64). A represents parautochthonous lower Paleozoic shelf strata overlying the poorly reflective Grenville basement, B, C, F, and E denote large antiforms, R is an eastern ramp, D is a Mesozoic dike swarm, M is Moho, BRT is Blue Ridge master decollement, DT is deeper detachment, TS is transported Taconic suture, BDT is the brittle-ductile transition zone, and E represents east-dipping Alleghanean and earlier shear zones and thrusts. The circles represent projected hypocenters of previously recorded earthquakes (Coruh et al., 1988).

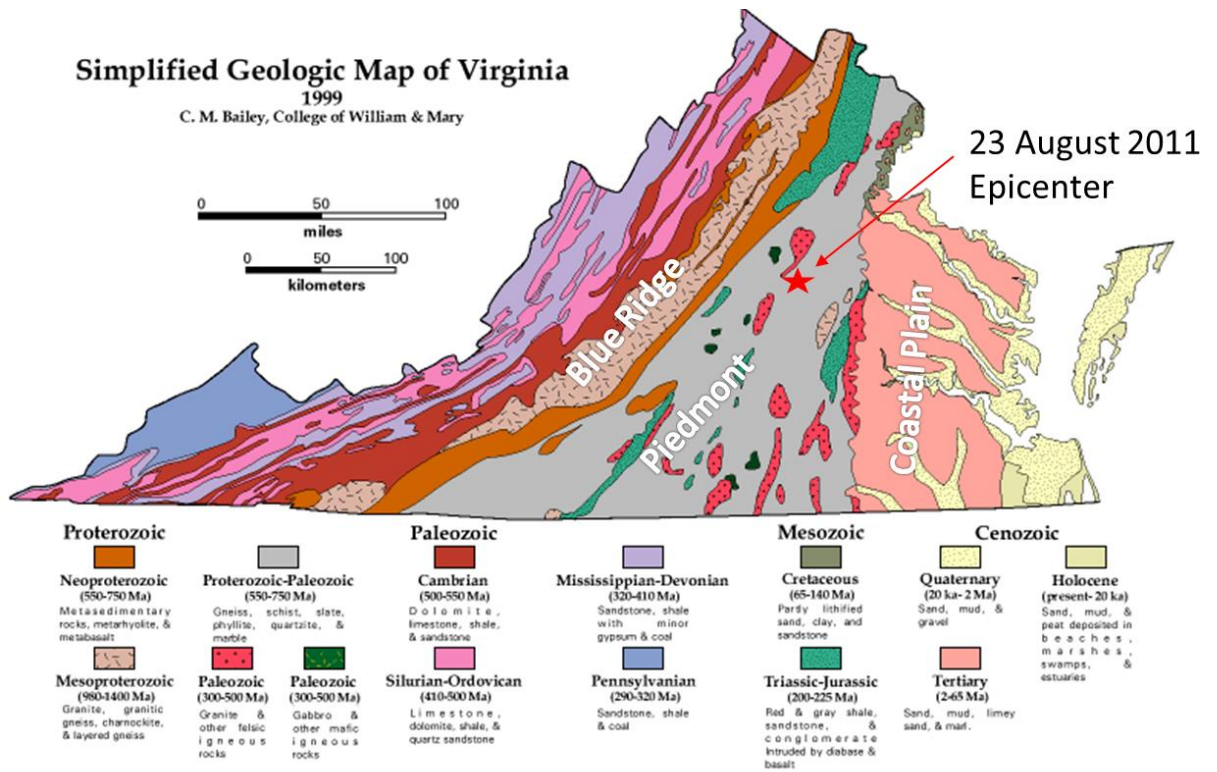


**Figure 3:** The 23 August 2011 Mineral, Virginia, earthquake epicenter is shown by the red star in the Piedmont province (Bailey, 1999a).

Crustal thickness underneath Mineral, Virginia is approximately 35 to 40 km with the brittle-ductile transition zone occurring at depths ranging from 12 km in the western CVSZ to 19 km in the east (James et al., 1968; Coruh et al., 1988; Figure 2). The bedrock of the CVSZ is comprised of a complicated structure of tectonically accreted allochthonous crystalline terrains (Pratt et al., 1988; Figure 3). The tectonic history of the region includes both Late Paleozoic compression and Early Mesozoic extension due to continental collision and breakup events that created numerous decollements, detachments, reverse and normal faults (Bollinger and Sibol, 1985; Coruh et al., 1988; Chapman, 2013). The hypocenter of the 2011 Mineral, Virginia, earthquake has been located west of the northeast-trending Spotsylvania thrust fault, which separates the

western Cambrian-Ordovician volcanic-plutonic Chopawamsic terrane from the eastern Proterozoic granulite Goochland terrane (Kim and Chapman, 2005; Figures 4 and 5).

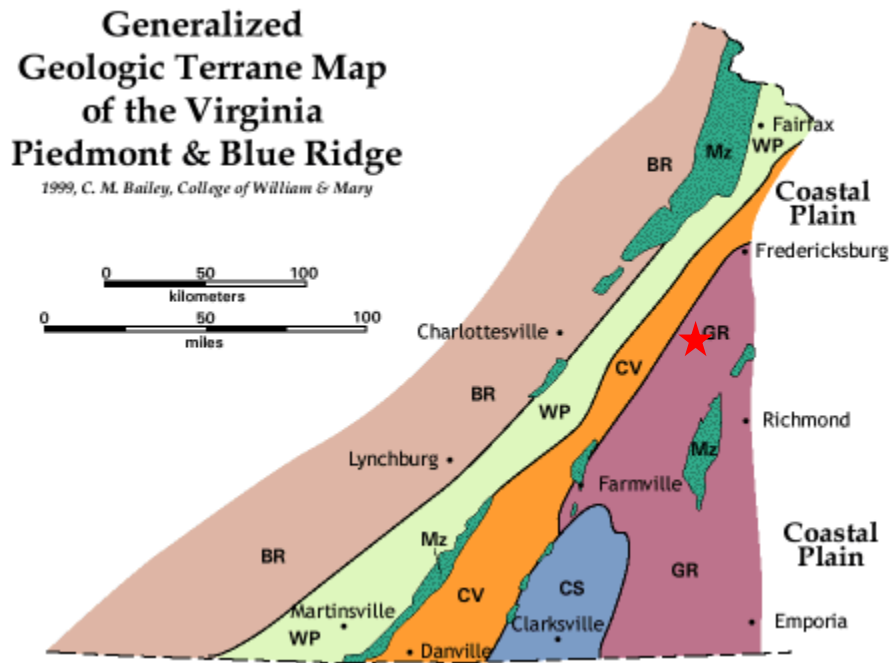


**Figure 4:** Generalized geology of the Virginia Piedmont. MZ: Mesozoic Basins, BR: Blue Ridge, WP: Western Piedmont, CV: Chopawamsic Volcanic Belt, CS: Carolina Slate Belt, and GR: Goochland Raleigh Belt. The red star is the approximate location of the 2011 mainshock (Bailey, 1999b).

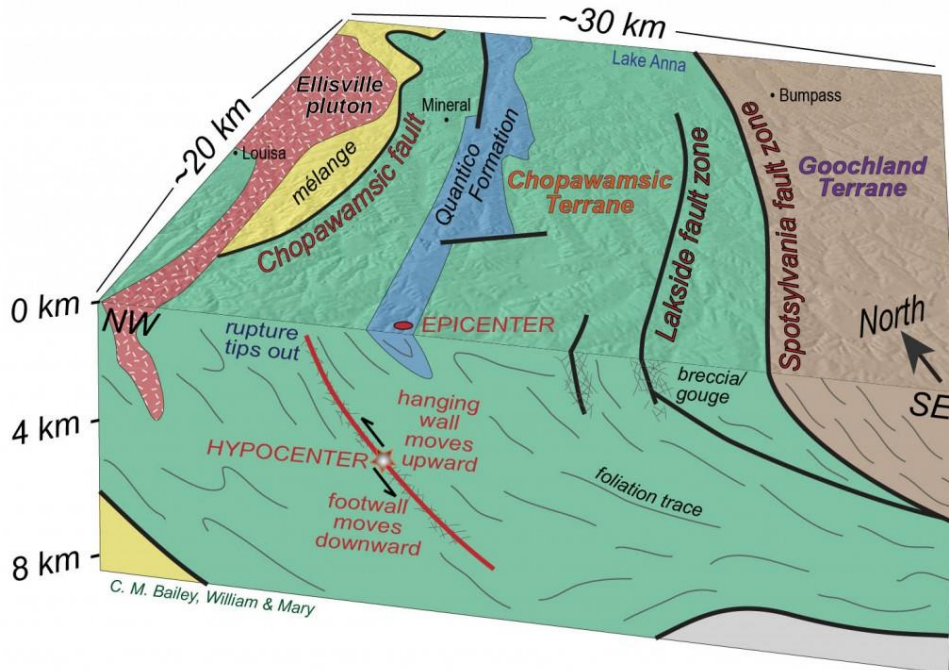


**Figure 5:** Map and cross-sectional view of the mainshock location. The event has been attributed to a thrust fault in the Chopawamsic terrane between the Chopawamsic and Spotsylvania faults (Bailey, 2011).

The Chopawamsic terrane consists of the remnants of a volcanic arc that accreted to Laurentia during the Late Ordovician Taconic orogeny (Bailey, 1999a; Figure 6). Following the Taconic orogeny was the collision of Acadia with Laurentia in the Late to Middle Devonian Acadian Orogeny, which had marginal effect on the northcentral Appalachian region (Faill, 1998; Figure 6). The last and most significant compressional event to affect the central Appalachians was the Late Paleozoic Alleghenian orogeny (Faill, 1998; Figure 6). This continent-continent collision between Laurasia and Gondwana created numerous low-angle thrust faults and reactivated older low-angle thrust faults of Taconic age (Chapman, 2013; Faill, 1998). The three main thrust faults in the CVSZ that formed during Alleghenian orogeny are the Chopawamsic fault, the Spotsylvania fault, and the Hylas fault zone (Figure 7). The Goochland terrane was thrust westward by the northeast-trending, southeast-dipping Spotsylvania thrust fault, now juxtaposed against the Chopawamsic terrane (Kim and Chapman, 2005). Early Triassic rifting caused normal faulting on the reactivated Alleghenian thrust faults and the development of numerous rift basins as the African and North American continents began to separate (Coruh et al., 1988; Withjack et al., 1998; Kim and Chapman, 2005; Chapman, 2013; Figure 6).

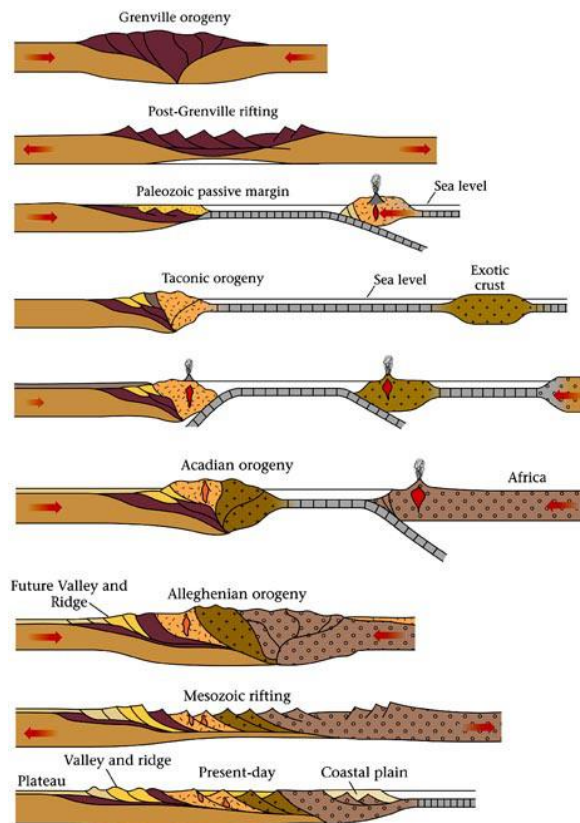


**Figure 6:** The tectonic history of the CVSZ involved many extensional and compressional events. The Taconic orogeny involved the accretion of the volcanic island arc Chopawamsic terrane in a compressional environment. The Acadian orogeny had little effect on the CVSZ as the accretion occurred in the northeast United States. The Alleghenian orogeny involved the continent-continent collision of Gondwana and Laurentia and was followed by Mesozoic rifting. The eastern United States is now a passive margin. (Bentley, 2010).

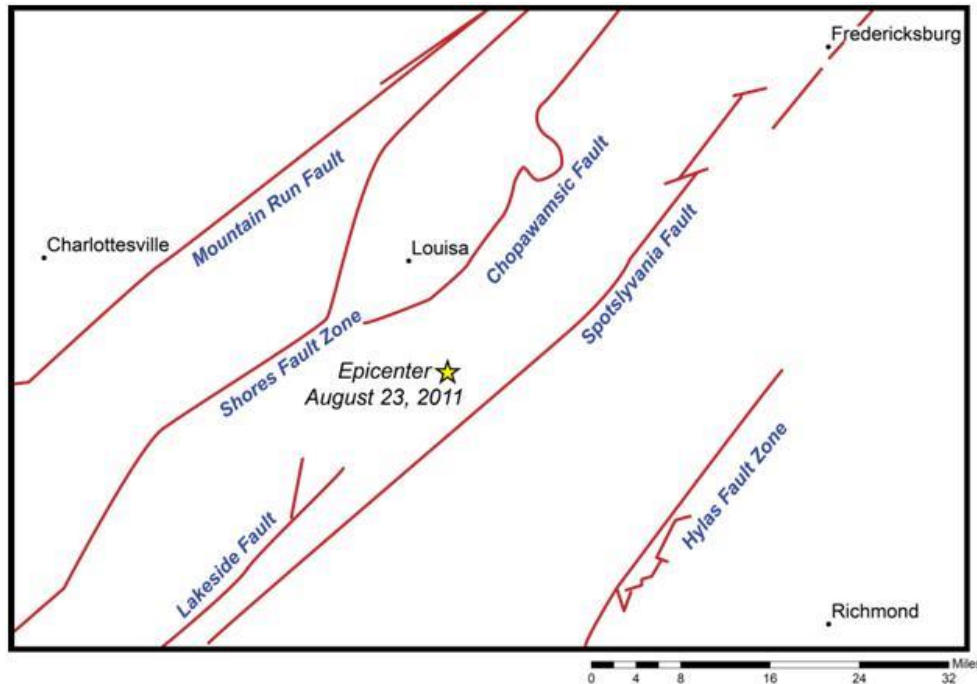


**Figure 7:** Map view of the main faults near the 2011 earthquake epicenter. Figure from Virginia Division of Geology and Mineral Resources, DMME.

Rifting ceased in the Early Jurassic when the eastern United States entered a transitional period from rift to drift, during which northwest striking dikes and diabase sills intruded the previously emplaced rock formations and extrusional basalt flows formed on the Earth's surface (Withjack et al., 1998). Upwelling of the asthenosphere in the middle of the rift resulted in crustal shortening in eastern North America, leading to the formation of northeast striking thrust faults due to the northwest-southeast orientation of the maximum horizontal stress axis (Withjack et al., 1998; Kim and Chapman, 2005).

Sea-floor spreading centers developed in the Early Cretaceous, creating a compressional stress regime with a maximum compressional stress axis trending east-west that is still present to this day (Stein et al., 1989; Kim and Chapman, 2005). Ridge-push forces due to cooling of the lithosphere created at the Mid-Atlantic Ridge oppose the continental drag forces created by the basal drag friction between the continental

lithosphere and the asthenosphere below the North American plate (Zoback and Zoback, 1989). This regional east-west maximum compressional stress is thought to be the primary force creating earthquakes in the CVSZ, which are considered to be compressional reactivations of favorably-oriented faults that were created during past episodes of tectonic activity (e.g., Wolin et al., 2012; McNamara et al., 2014a; Zoback and Zoback, 1989).

### Past Work

Initial studies of the 23 August 2011 main event and early aftershock sequence have placed the mainshock rupture at a depth of 8 km, the mean depth determined for previous CVSZ earthquakes (Chapman, 2013). The 2011 mainshock occurred on a thrust fault having a strike and dip of  $N36^{\circ}E \pm 12^{\circ}; 49.5^{\circ}SE \pm 6^{\circ}$  (McNamara et al., 2014a),  $N29^{\circ}E; 51^{\circ}SE$  (Chapman, 2013), or  $N28^{\circ}E; 50^{\circ}SE$  (Herrmann, 2011; Figure 5). Numerous seismometers were deployed surrounding the epicentral area to record the aftershock sequence in the immediate hours and days following the mainshock (McNamara et al., 2014b). A dense network of seismometers closely surrounding an aftershock sequence reduces the location error of event hypocenters and increases the probability of detecting smaller magnitude aftershocks. The fault plane mapped from the early aftershock hypocenters located by Chapman (2013) is approximately 0.75 km above the fault plane determined for the mainshock, suggesting that these aftershocks may have been located on an adjacent, parallel fault (Figure 8). Other studies have found that some aftershock clusters favored locations near the intersections of Jurassic dikes and pre-existing faults (Shah et al., 2015). Shah et al. (2015) also suggest the influence of local

stresses resulting from variations in rock density and rheology as important forces contributing to CVSZ seismicity.

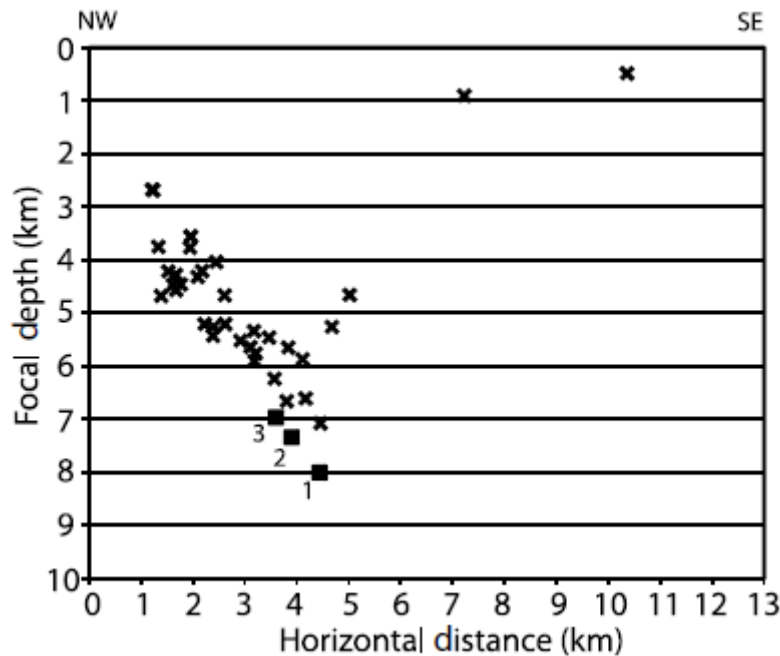


**Figure 8:** Early aftershock events located by Chapman (2013) with the mainshock subevents labeled 1-3 in order of occurrence. The mainshock subevents are located at the southwest end of the aftershock zone and appear to occur on a deeper fault structure with a similar dip as the plane delineated by the aftershock sequence (Chapman, 2013).

Recent surficial geologic mapping in the CVSZ has extended known faults and identified new faults in the epicentral area (Burton et al., 2015; Hughes et al., 2015; Figures 9 and 10). Hughes et al. (2015) identified a zone of high strain in the Chopawamsic Formation and mapped a southwest extension of the oblique-thrust Long Branch Fault (Figures 9 and 10). Two faults showing evidence of post-Paleozoic faulting were discovered in the epicentral area near the eastern margin of the Ellisville Pluton and have similar strikes and dips as those calculated for the 2011 mainshock (Burton et al., 2015; Figure 10). The Harris Creek Fault trends N50°E and is one continuous structure whereas the N30°E trending Roundabout Farm Fault is one of many similarly trending faults (Burton et al., 2015; Figure 10). Both faults show evidence of post-Paleozoic thrust

and strike-slip faulting with strikes and dips similar to those from the focal mechanisms determined for the main event and its subsequent aftershocks (Herrmann, 2011; Chapman, 2013; McNamara et al., 2014a). Improved resolution of fault structure geometry using the relative location scheme of Ebel et al. (2008) and the moment tensor inversion technique of Ebel and Bonjer (1990) can assist future geologic mapping excursions in an effort to locate a possible surface projection of the seismogenic structure.

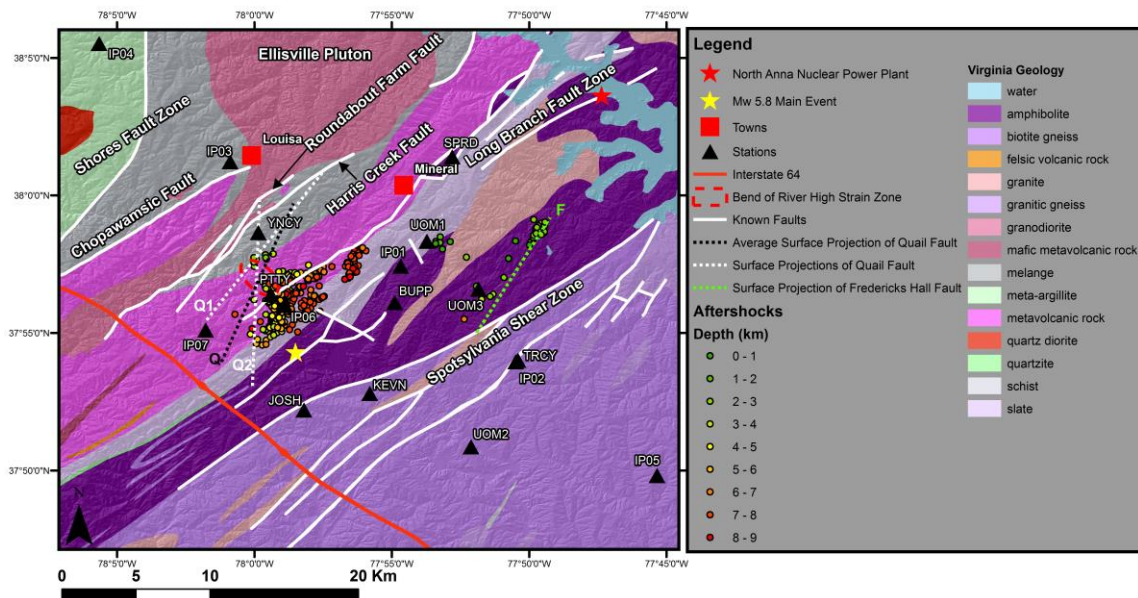


**Figure 9.** Map view of the Mw 5.8 Mineral, VA, earthquake and aftershock sequence. Only relative hypocenters with a location uncertainty of one standard deviation ( $\sigma$ ) < 0.1 km are shown. Simplified Virginia geology (Dicken et al., 2005) is shown overlying a shaded hillslope generated from a Lidar DEM. North Anna Nuclear Power Plant is located approximately 22 km northeast of the center of the aftershock cluster. Stations used in the relative location and moment tensor inversion analyses are shown. Various surface projections of the Quail Fault (Q, Q1, and Q2) and Fredericks Hall Fault (F) are represented by the dashed lines and were calculated using a plane of best-fit. Q1 is the surface projection resulting from using only aftershock hypocenters from the northeastern portion of the main fault whereas Q2 is the surface projection resulting from using only hypocenters from the southern portion of the main fault. Q is the plane of best-fit surface projection using all of the aftershock hypocenters from the main fault. The strikes and dips of the planes used to project Q1, Q2, and Q are 045°/67°, 002°/72°, and 025°/68°, respectively. The strike and dip of the plane used to project F are 033°/85°. Virginia fault, geology, and DEM data were sourced from the USGS. Fault locations were updated according to findings from Burton et al. (2014), Burton et al. (2015), and Hughes et al. (2014).

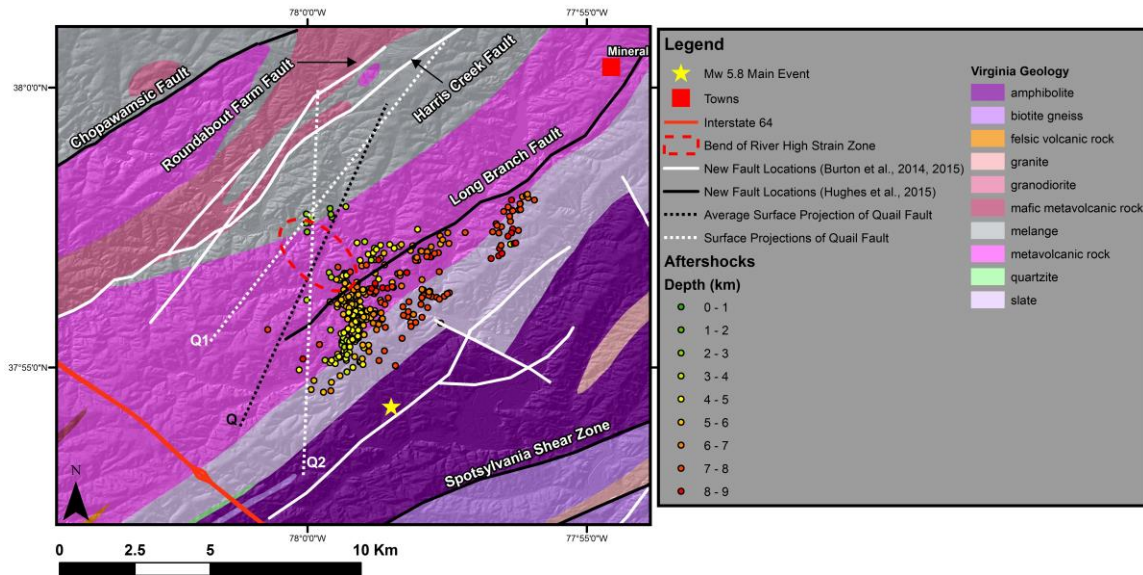


**Figure 10.** Zoomed-in version of Figure 9 emphasizing the similarities in the strikes of the fault planes illuminated by the Mw 5.8 Mineral, VA, aftershock sequence and the new fault locations determined by Burton et al. (2014) and Burton et al. (2015). Only relative hypocenters with a location uncertainty of one standard deviation ( $\sigma$ ) < 0.1 km are shown. Simplified Virginia geology (Dickens et al., 2005) is shown overlying a shaded hillslope generated from a Lidar DEM. Various surface projections of the Quail Fault (Q, Q1, and Q2) are represented by the dashed lines and were calculated using a plane of best-fit. Q1 is the surface projection resulting from using only aftershock hypocenters from the northeastern portion of the main fault whereas Q2 is the surface projection resulting from using only hypocenters from the southern portion of the main fault. Q is the plane of best-fit surface projection using all of the aftershock hypocenters from the main fault. The strikes and dips of the planes used to project Q1, Q2, and Q are 045°/67°, 002°/72°, and 025°/68°, respectively. Virginia fault, geology, and DEM data were sourced from the USGS. Fault locations were updated according to findings from Burton et al. (2014), Burton et al. (2015), and Hughes et al. (2014).

## METHODS

### Relative Locations

Earthquakes from the aftershock sequence (“secondary” events) were located relative to spatially and temporally well-constrained “master” events using a modified version of the double-difference earthquake location scheme of Waldhauser and Ellsworth (2000). Following the technique outlined in Ebel et al. (2008), cross-correlation was used to determine precise arrival-time differences of body waves for the master event versus a secondary event at common stations surrounding the epicentral area. The

differences in the P and S travel times for the two events at a common set of stations were used to calculate the offset in hypocentral location of the secondary event relative to the master event (Waldhauser and Ellsworth, 2000).

A jackknife analysis was used to calculate uncertainties in the relative location parameters. The jackknife method involves resampling a dataset numerous times while systematically omitting individual observations per resample in order to determine the relative influence of each observation on the dataset as a whole. Stations that contributed to the relative location uncertainty were also identified as part of the jackknife analysis. When the root mean square (RMS) error between the predicted and computed relative arrival times has been reduced to less than two times the sampling period of most stations (0.02 s), no further resolution of the relative location of the hypocenter is possible. Thus, the smallest uncertainties in the relative location hypocenters is about 120 m assuming a digital sampling period of 0.01 s and a P-wave velocity of 6.09 km/s for the hypocentral region.

The relative location analysis was carried out for all secondary events that have absolute hypocentral locations near the master event to calculate the relative locations of a “cluster” of secondary events around the master event. Multiple master events with absolute locations in different parts of the aftershock zone, along with their associated clusters of secondary events, were used due to the large spatial extent of the seismicity following the mainshock in order to increase the probability of finding low-uncertainty relative locations for the nearby secondary events. This method improves the locations of the secondary event hypocenters relative to the location of the corresponding master event, allowing for a high-resolution analysis of the geometry of the seismogenic

structure on different parts of the fault. The drawback of the method is that it does not improve the absolute locations of the events, and hence the resulting pattern of seismicity might be offset from the subsurface fault structure that it is intended to image. In order to better constrain the relative locations of two different but nearby clusters of events for which relative locations had been calculated, a secondary event from the edge of each relative location cluster and close to the other cluster was selected, and the relative locations of these two secondary events were calculated. The result of this calculation allowed the relative locations of the two clusters to be precisely computed.

Several assumptions were made in the application of the relative-location method of Ebel et al. (2008). The master and secondary events are assumed to have similar focal mechanisms, implying that the P and S waves that arrive at each station for the two events take off from similar locations on the body-wave radiation patterns from each source. Ray paths from the master event and secondary event to a common station are assumed to be similar, and thus the waveforms from both events would experience the same scattering and frequency attenuation when recorded at a given station. The velocity structure in the hypocentral region that encompasses both the master and secondary events is assumed to be uniform, and any minor deviations in the ray paths to a given station for the two events are assumed to cause only small differences in the waveforms of the two events given the station sampling frequency of 100 or 200 Hz.

Waveform data collected by the Virginia Tech XY, IRIS Ramp YS, and USGS SY deployments of aftershock monitoring seismic stations were used in this study (Figure 9). Data from the strong-motion accelerometers deployed as part of the aftershock survey were not used in this study. Absolute aftershock locations of 1600 events provided by

Virginia Tech were used to create multiple “clusters” that each contained one master event and tens to hundreds of possible secondary events for use in the relative location analysis (Figure 11). A two-layer crustal velocity model developed for the Central Virginia Seismic Zone (CVSZ) (Bollinger et al., 1980; Chapman, 2013) was used to determine the relative hypocenter locations.

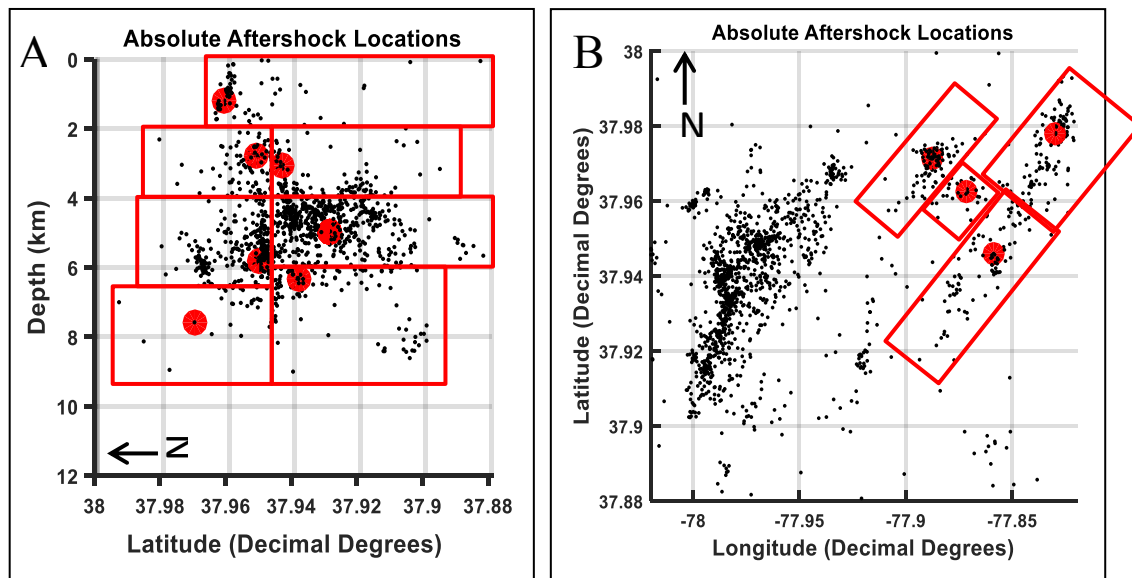


**Figure 11.** Figure A is a cross-sectional view of the absolute aftershock locations on the main fault looking east into the page. Figure B is a map-view of the main fault and the seismicity to the northeast. Each red box indicates the area from which secondary events that were relocated relative to a particular master event (red circles) were selected. The master event that was picked from the center of seismicity in each red box had a high signal-to-noise ratio and was well-recorded on as many stations as possible.

As noted above, due to the relatively large spatial extent of seismicity both along strike and down dip on the main aftershock zone, multiple clusters, each with one master event and surrounding secondary events, were formed, and a separate relative location analysis was carried out for the events in each cluster (Figure 11). The purpose of this was to maximize the chances that high-precision relative locations could be computed. An event near the center of each cluster that had a high signal-to-noise ratio and was well-recorded on as many stations as possible was chosen as the master event (Figure

11). The secondary events in a cluster were individually analyzed with the master event to determine if an accurate relative location of each secondary event relative to the master event could be calculated. For each master event-secondary event pair that was analyzed, a second-order zero-phase infinite impulse response filter (2-10 Hz passband) was used to filter the signals before processing in the relative location analysis. Time windows encompassing the arrival times of the P waves (0.1s before to 0.3s after the hand-picked P-wave arrival) on the vertical component and S waves (0.5s before to 1.5s after the hand-picked S-wave arrival) on all three components were created for the master event and the secondary event. These time windows were used in a cross-correlation to find the time shift with the maximum similarity between the master event and secondary event P and S waveforms at a common station (Figure 12). Normalized cross-correlation coefficients (C-values) greater than 0.6 were determined to represent cross-correlations with a high degree of similarity between waveforms, and therefore cross-correlations of body waves at a common station with C-values less than 0.6 were not used to calculate relative locations (Figure 12). Of the three station components for which S-wave cross-correlations were performed, the component with the largest C-value greater than 0.6 was used to calculate the S-wave arrival time difference between the master event and the secondary event (Figure 13).

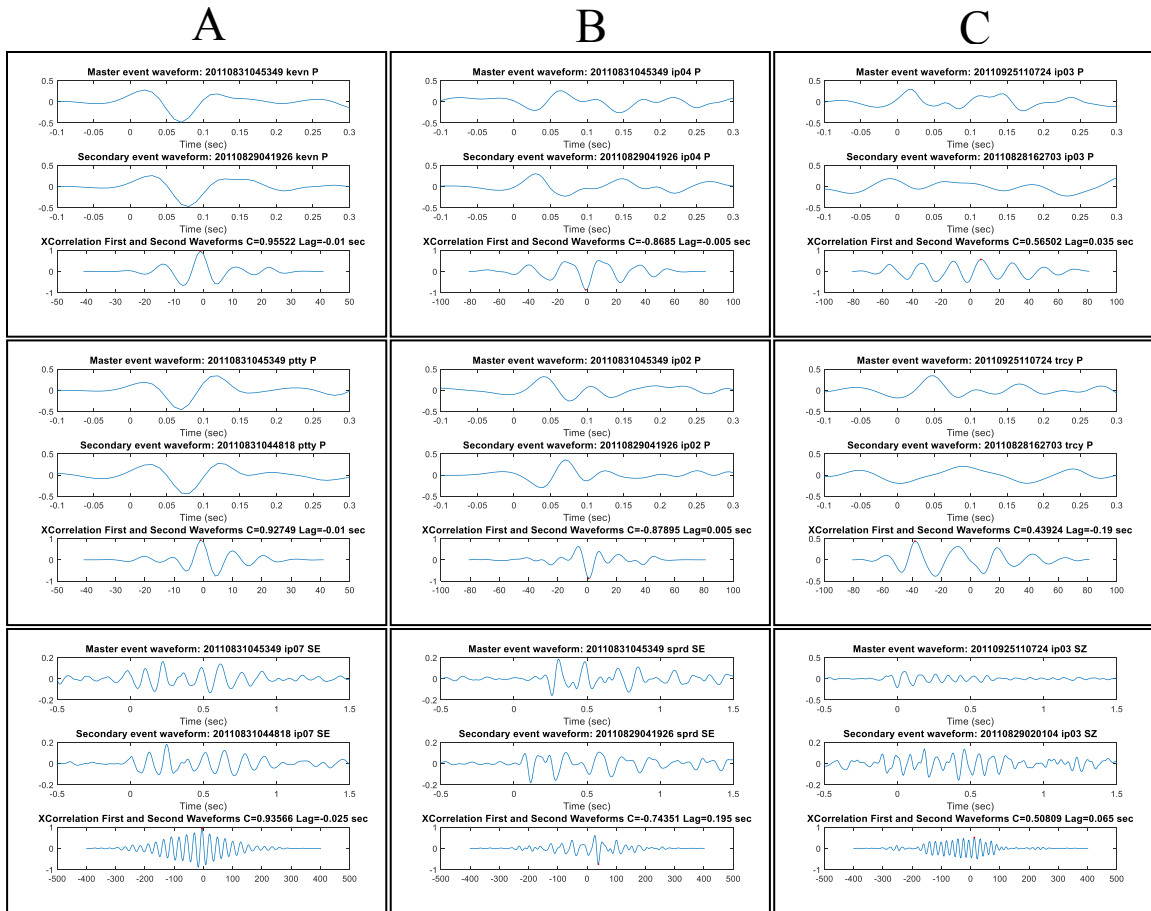


**Figure 12.** Examples of cross-correlations between master and secondary events. Each subplot displays master event and secondary event waveforms from the same station and component in addition to normalized cross-correlation coefficients at different lag times. C is the maximum normalized cross-correlation coefficient calculated at the time shift (labeled Lag in the heading of the third plot for each pair of events that are correlated). Column A shows examples of events with high positive C-values, column B shows events with opposite waveform polarity and high negative C-values, and column C shows events with low C-values ignoring the sign of the C value ( $|C| < 0.6$ ). Lag times from cross-correlations in columns A and B were used in relative location calculations whereas the data for events pairs like those in column C were not used to compute the relative locations.

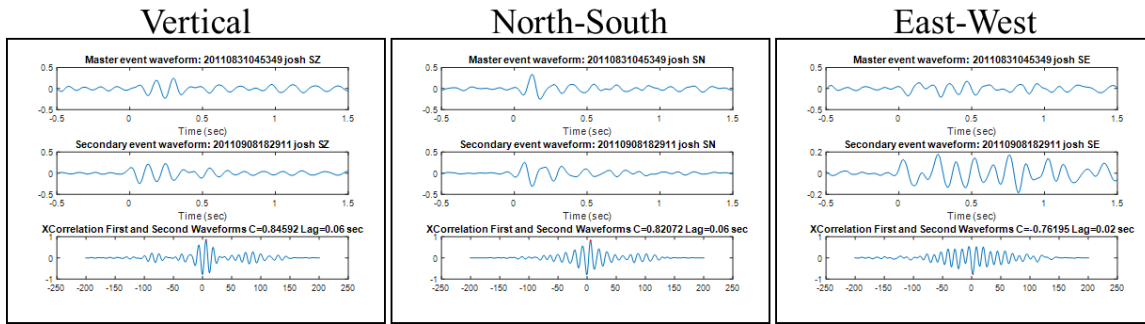


**Figure 13.** Cross-correlation results for a master event and secondary event S wave at station JOSH. The cross-correlation was performed for waveforms using all three components, and in this case resulted in absolute C-values  $> 0.6$  for each component. The cross-correlation of waveforms recorded by the vertical component resulted in the largest absolute C-value for the S-wave cross-correlation at this station and was used in the calculation of the relative location whereas the North-South and East-West components were not. In this case, the cross-correlation of the master event and secondary event S waves recorded by the North-South component resulted in the same lag time as those associated with the maximum absolute C-value on the vertical component, which added confidence that an accurate S-wave lag time had been found.

Some secondary event waveforms showed similar shapes but with opposite polarities compared to the master event waveforms, resulting in large negative C-values determined in the cross-correlations. For this reason, the maximum absolute C-values were used to determine the lag time of the secondary event waveform relative to the master event waveform in order to include the opposite polarity cross-correlation results (Figure 12). In some cases, the waveforms for the master event, secondary event, or both were very sinusoidally shaped, which resulted in many cross-correlation peaks of similar values at different lag times (Figure 14). For these cases, it was unclear whether the maximum C-value represented the proper shift between the master event and secondary event even though the maximum C-value was greater than 0.6. Under these circumstances, the station and phase were not used for the relative location analysis due to this uncertainty in the correct lag time (Figure 14). The lag times associated with the maximum C-values for body-wave cross-correlations at each station surrounding the events that passed the acceptance criteria described here were used to calculate the relative arrival time differences for the relative location analysis.

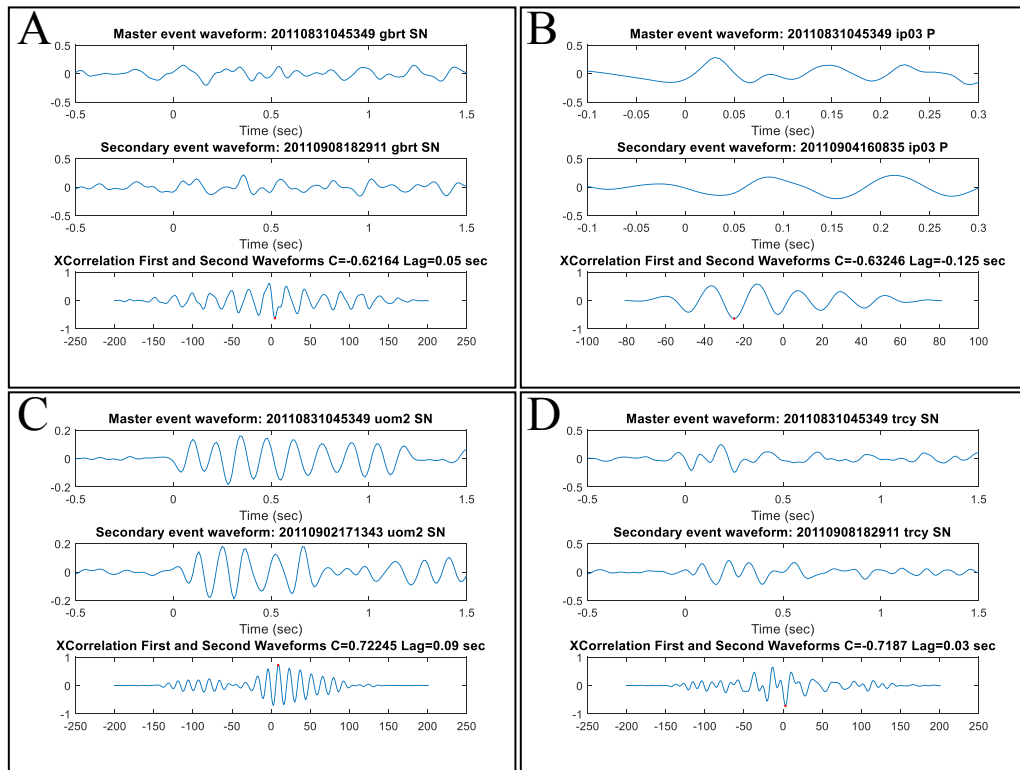


**Figure 14.** Examples of normalized cross-correlation coefficients (C-values)  $> 0.6$  that were not used in the relative location analysis. Figures A-D show examples of situations where multiple lag times correspond with C-values of similar magnitudes. Figures C and D show examples of lag times that resulted in a maximum absolute C-value  $> 0.6$  when the secondary event waveform is shifted to the right relative to the master event waveform. The appearance of the first arrivals of these waveforms suggests that there should be a negative lag time that shifts the secondary event waveform to the left relative to the master event waveform.

The relative location method summarized above was used to relocate 880 events with RMS errors for the relative locations below about 0.02 sec, which indicates that the maximum possible precision of these relative locations was achieved. Relative locations for secondary events in a cluster around individual master events were computed, and then the relative locations of pairs of events from different clusters were used to find accurate relative locations of the different clusters relative to each other. Thus, effectively every master event on the main fault structure was relocated relative to one well-defined master event using the relative location method. This produced an accurate reconstruction of the main fault structure based on only one master event absolute location. The

resulting relative location hypocenters revealed trends in seismicity that were not apparent from absolute hypocenter locations alone, illuminating some major seismicity lineations within the main zone of aftershocks (Figure 15). These are interpreted as two larger fault planes and one smaller fault plane, and for each of these a plane of best-fit was computed through the trend of the seismicity that is interpreted to lie along that fault plane (Figures 16 and 17). Also shown on Figure 16 is a single plane that is fit through all of the aftershocks in this primary aftershock cluster. Off-fault hypocenters near the intersection of the primary fault planes were not used in the calculation of the geometry of the primary fault planes in Figures 16 and 17 to ensure that accurate strikes, dips, and surface projections of each interpreted plane could be determined.

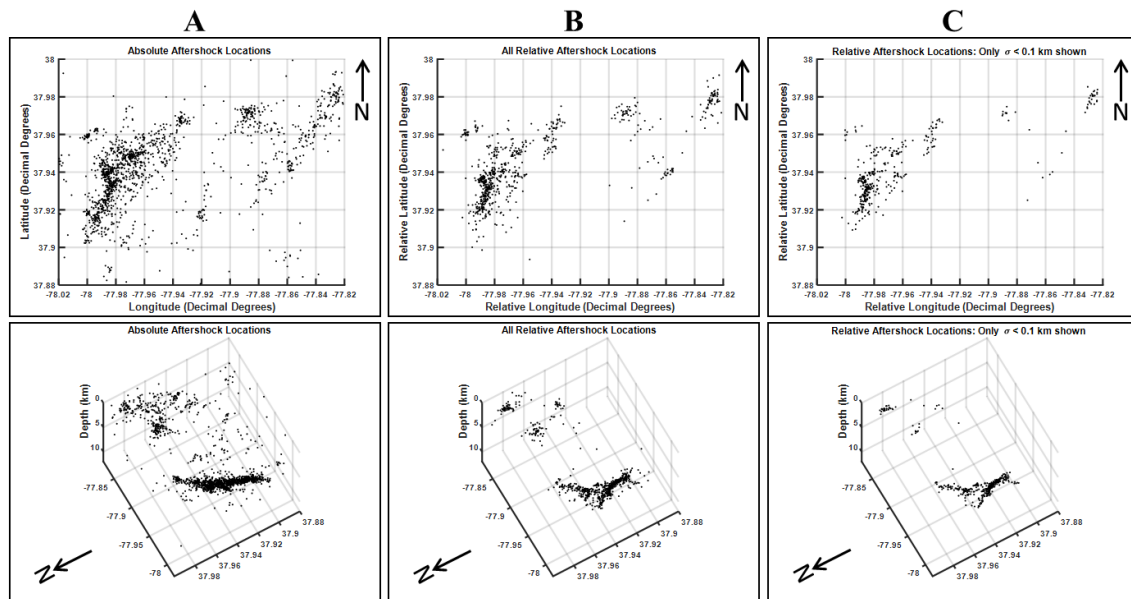


**Figure 15.** Comparison of absolute aftershock locations (column A), relative aftershock locations (column B), and relative aftershock locations with  $\sigma < 0.025$  sec (column C). The top row is a map view of aftershock epicenter locations and the bottom row is an oblique view down-dip of the main fault structure. Many of the events east of the main fault had poorly constrained relative locations due to the lack of stations east of these events.

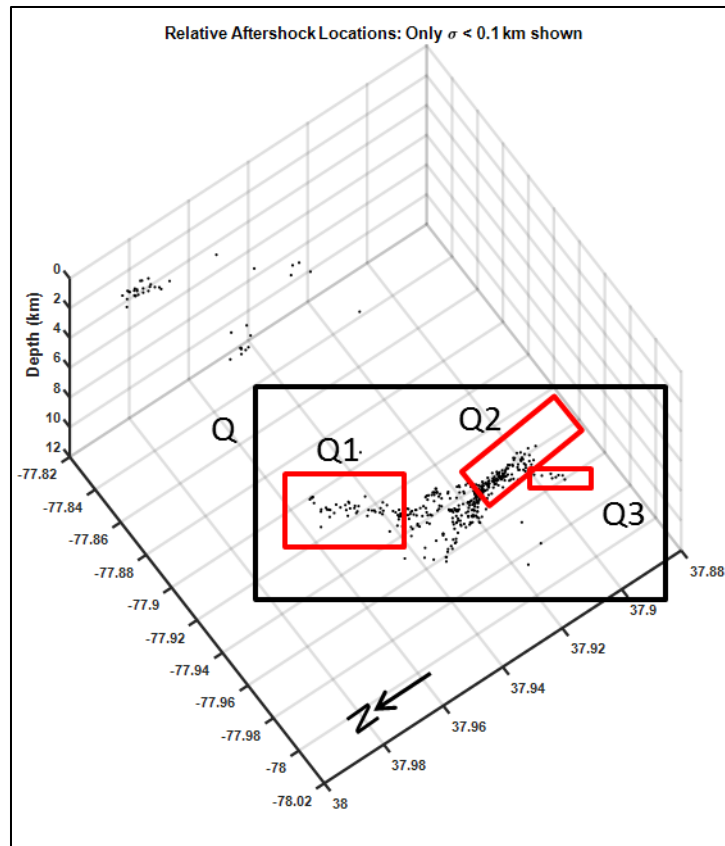


**Figure 16.** Major linear trends in the seismicity in the most active aftershock zone are outlined by the red boxes. A plane of best-fit was created individually for Q1, Q2, and Q3 using the events shown in each respective red box. All of the events in the black box labeled Q were used to calculate a plane of best-fit to represent the main fault as a single planar feature. Surface projections of Q1, Q2, and Q are shown in Figures 9 and 10.

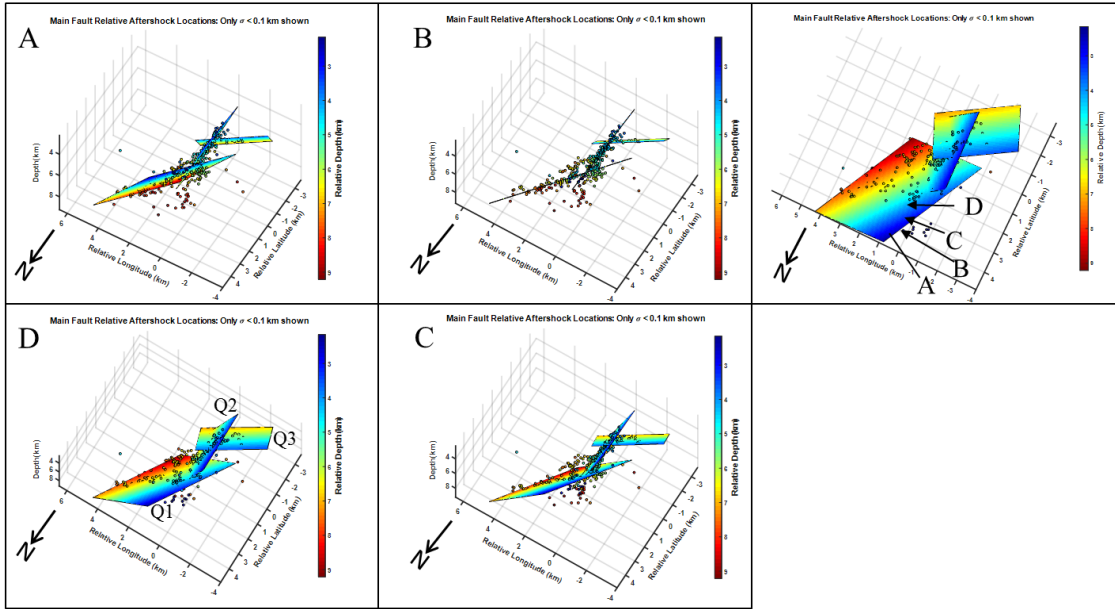


**Figure 17.** Oblique map views of the main fault structure and planes of best-fit calculated for each visually identified linear trend in seismicity. View A shows planes Q1 and Q3 through the northwest footwall, view B is a down-dip view of the main fault planes, view C is looking down on the fault planes through the head wall, and view D is an oblique map view. The figure on the right shows vectors normal to the oblique map view represented in images A-D. Only relative hypocenters with a location uncertainty of one standard deviation ( $\sigma$ )  $< 0.1$  km are shown. Planes and hypocenters are colored by depth. Most seismicity occurs along planes Q1 and Q2 with some off-fault seismicity near where these two planes intersect. Much less seismicity occurs along plane Q3 which has a similar strike and dip as plane Q1. The strike and dip of planes Q1, Q2, and Q3 are  $045^{\circ}/67^{\circ}$ ,  $002^{\circ}/72^{\circ}$ , and  $056^{\circ}/58^{\circ}$ , respectively.

## Moment Tensor Inversion

Focal mechanisms were determined for a number of aftershocks at various locations in the aftershock zone using the moment tensor inversion method of Ebel and Bonjer (1990). First-motion amplitudes and polarities were read from the direct P waves at stations surrounding the event. S waves were rotated so that the amplitudes from the transverse components of the direct S waves could be read (SV waves were past the critical angle at the surface and so could not be used in the analysis). The instrument gains were used to convert the P and SH amplitudes to ground-motion amplitudes. The

ground-motion amplitude data were input into a linear least-squares inversion to calculate the five independent components of a traceless moment tensor that best predicts the observed amplitudes and polarities. The resulting moment tensor was decomposed into the largest possible double-couple moment tensor and a residual compensated linear vector dipole (CLVD) moment tensor. The source moment, strike, dip, and rake were calculated from the double-couple. An additional non-linear least-squares inversion code was used to find seismic moment, strike, dip, and rake values that optimize the fit between the observed amplitudes and those calculated from the double-couple solution.

This method was only appropriate for small magnitude events due to the assumption that the source time function (STF) is so short in duration that it can be represented by a Dirac delta function (Ebel and Bonjer, 1990). Some other assumptions and limitations are part of the application of this moment tensor inversion method (Ebel and Bonjer, 1990). The seismic velocity structure between all sources and receivers was assumed to be the same for all events, and anelastic attenuation was assumed to be so small that it could be ignored in the analysis. All stations were located at far-field distances from the source, and only direct body waves were used in the moment tensor inversions to avoid distortion from reflected and refracted waveforms.

The seismic network data and velocity model used for the relative location analysis were also used in the moment tensor analysis. Focal mechanisms were determined for events that had been relocated using the relative location method so that nodal plane orientations of the focal mechanisms could be compared with trends in the seismicity near the aftershock locations.

Many independent tests were conducted to determine the accuracy of the focal mechanisms found using the moment tensor inversion method. Initially, inversions using only P-wave first-motion amplitudes were performed because the initial P-wave amplitudes were relatively easy to identify on many of the station seismograms. S-wave first arrivals can be masked by scattered P waves and P-to-S wave conversions, making a clear S-wave first arrival difficult to determine (Ebel and Bonjer, 1990). Thus, as a first step in the focal mechanism procedure, P-wave only inversions were performed using first-motion amplitudes read from common stations for events with small offsets in relative hypocentral locations, and the resulting focal mechanisms were compared to determine if the different events had similar double-couple solutions (Figure 18). S-wave first-motion amplitudes at common stations were then included in the inversion to determine whether the focal mechanisms found using both P- and S-wave amplitudes were similar to the focal-mechanism solutions using only P waves for the same events (Figure 18). S-wave first arrivals at stations closer than 3 km from the hypocenter were not used because the uncertainty in the hypocentral location can lead to large uncertainties in the rotation of the horizontal components to SV and SH ground motions. Also, small shifts in the hypocentral location could result in large changes in station take-off angle on the SH-wave radiation pattern.

In many cases, the addition of the S-wave amplitudes caused little change in the focal mechanisms relative to the P-wave only inversion, or they caused a rotation of the nodal planes relative to the P-only solution that was consistent among all events with nearby hypocenters (Figure 18). Additional body-wave amplitude picks at stations that were not common among the events with small offsets in hypocentral locations were then

included in the inversion to further test the calculated focal mechanisms. The most accurate focal mechanisms are those that had little change in inversion results when independent data were included with common P- and S-wave stations, for which the RMS error between calculated and observed amplitudes was minimized and for which the CLVD component was less than 1/6 of the seismic moment.

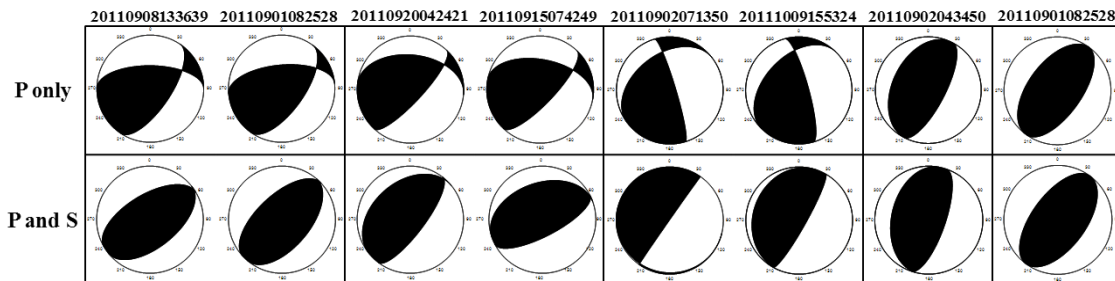


**Figure 18.** Focal mechanism analysis for pairs of events with small hypocentral differences determined from the relative location analyses. First motion P-wave polarity and amplitude picks from waveforms recorded at the same stations were identified for each pair of events and used in the moment tensor inversion. First motion S-wave polarity and amplitude picks from waveforms recorded at the same stations were then included with the P-wave picks in the moment tensor inversion. Similar focal mechanism solutions generated by P-wave picks between the two events indicate that there was little variation in fault geometry and motion at the location of the two hypocenters. The focal mechanisms for the events were determined to be accurate when the inclusion of S-wave picks in the inversion resulted in a similar moment tensor to that for the P-wave only inversion result. Few P-wave picks in the P-wave only inversion generally resulted in a greater change in focal mechanisms when S-wave picks were included. This was likely due to sparse sampling of the P-wave radiation pattern by stations used in the P only inversion. The two events on the right show examples of focal mechanisms that experienced little to no change from P-wave only to P- and S-wave inversion results. The number above each column of focal mechanisms shows the year, month, day, hour, minute and second of the origin time of the event.

Accurate focal mechanism solutions could not be determined for every event analyzed using the moment-tensor inversion method. An anti-aliasing filter used to remove noise from the signal also appeared to create acausal noise before the P-wave, making the first motion difficult to determine for some stations, especially for low-amplitude P-wave first arrivals (Scherbaum, 1996; Scherbaum and Bouin, 1997; Figure 19). Also, the radiation pattern of events east of the main fault could not be constrained

due to the relatively limited azimuthal coverage of the focal spheres due to the locations of the events relative to the recording stations (Figure 9).

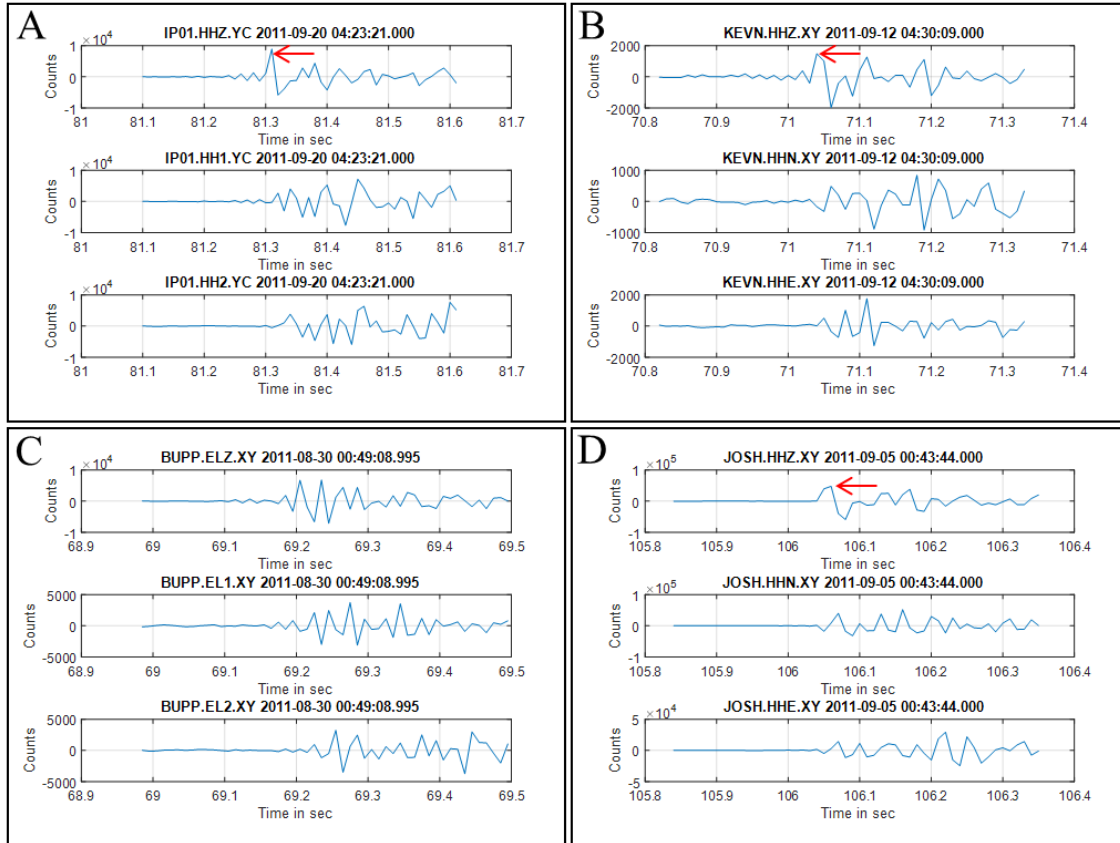


**Figure 19.** Examples of acausal noise before the first arrival of the P wave. All station components are shown but only P-wave amplitudes from the vertical component were used in the moment tensor inversion. Red arrows indicate the interpreted P-wave first motions. Figures A and B show examples of a first motion signal that was stronger than the acausal noise preceding it. Figure C shows an example of acausal noise obscuring the P-wave first motion to an extent that it was not used in the moment tensor inversion. Figure D shows an example of a P-wave first motion that was not contaminated by acausal noise.

Fifty-nine focal mechanisms were determined using the moment-tensor inversion method for events that had been relocated using the relative location method (Figures 20 and 21). Accurate focal mechanisms were created for events with hypocentral depths ranging from 2.45 km to 8.00 km and moment magnitudes ranging from 0.48 to 2.69. Uncertainties in the calculated strikes and rakes of the focal mechanisms in this study range from  $\pm 0.01^\circ$  to  $\pm 6.35^\circ$  whereas uncertainties in the calculated dips range from

$\pm 0.01^\circ$  to  $\pm 1.61^\circ$ . Focal mechanisms calculated for events on the two primary fault planes of the main fault structure generally depict thrust fault motion and have a nodal plane that corresponds closely with the fault planes delineated by the relative location hypocenters (Figures 20 and 21). Instances of normal-fault motion on planes with similar strikes and dips as nearby thrust focal mechanisms were calculated for two events on the main fault structure (Figures 20 and 21). In addition, normal faulting also occurred for several events that were located about 1-2 km northwest of the main aftershock zone (Figure 21). These events are located in the footwall block northwest of the main fault, and they seem to occur on a shallow planar feature and have similar strikes and dips as nearby thrust events on the main fault.

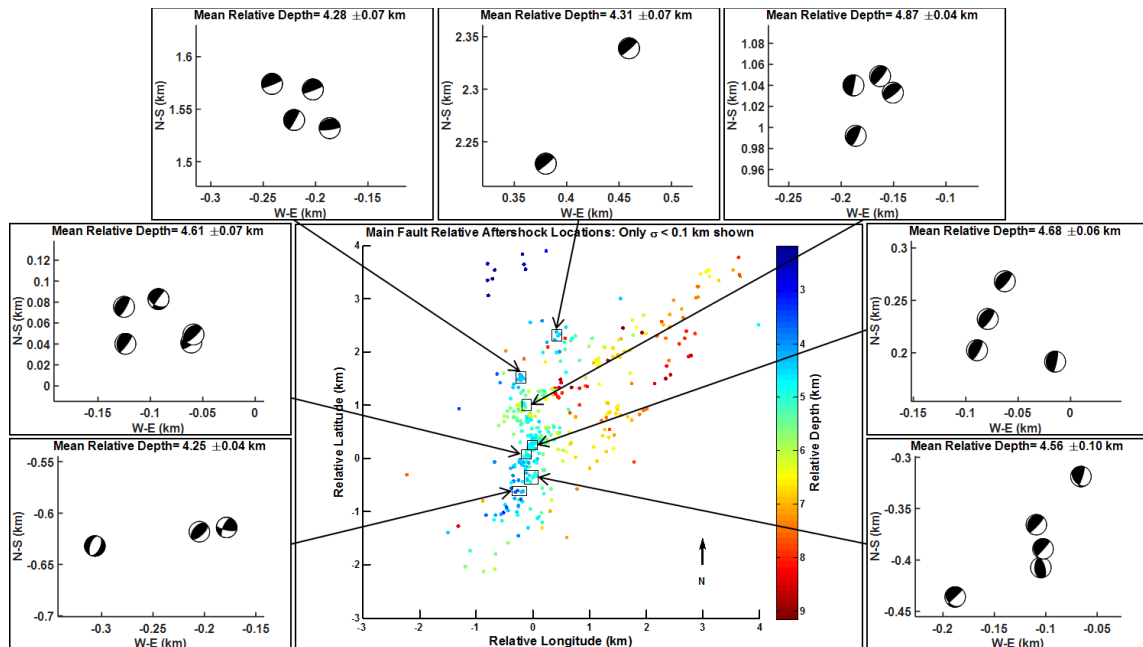


**Figure 20.** Map view of relative aftershock epicenters colored by depth. Clusters of aftershocks with small hypocentral distances are shown. Focal mechanisms calculated by the inversion of the source moment tensor are represented in map view. The focal mechanism plots in this figure all have the same vertical and horizontal scale to show relative epicentral distances, and the mean relative depth of the hypocenters is displayed above each plot. Focal mechanism solutions were compared to the trend of the aftershock hypocenters to determine which nodal plane is the probable fault plane. Focal mechanisms for the southern aftershocks depict a northeast striking fault dipping steeply to the southeast. Aftershock focal mechanisms show an increase in strike azimuth at more northern locations on the fault structure. The large majority of the aftershock focal mechanisms depict reverse fault motion.

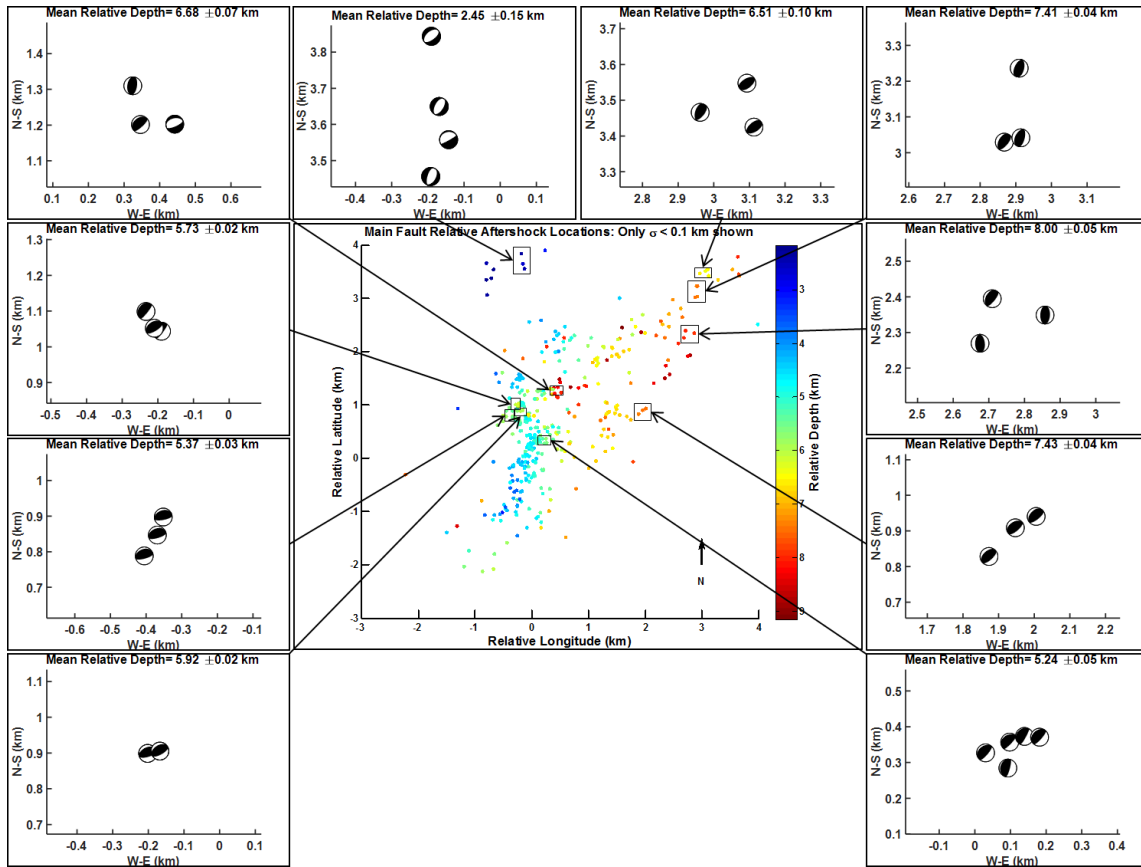


**Figure 21.** Map view of relative aftershock epicenters colored by depth. Clusters of aftershocks with small hypocentral distances are delineated by boxes. Focal mechanisms calculated by the inversion of the source moment tensor are represented in map view. The focal mechanism plots in this figure all have the same vertical and horizontal scale to show relative epicentral distances and the mean relative depth of the hypocenters within that box is displayed above each plot. Focal mechanism solutions were compared to the trend of aftershock hypocenters to determine which nodal plane is the probable fault plane. Aftershock focal mechanisms show a slight decrease in dip at deeper locations on the fault structure. Focal mechanisms located at a relative latitude of 1 km depict east-west trending features and are located at the juncture of two different striking and offset planar features. Deeper aftershocks show a northeast trending fault with reverse fault motion. The shallow cluster of aftershocks shown at the top of the figure depict normal faulting with similar strikes and dips as other focal mechanisms with deeper hypocenters. This shallow cluster is slightly offset to the northwest from the projected fault plane calculated from the deeper events. The offset locations of this shallow cluster help explain the difference in fault motion compared to the primarily reverse thrust trend in the primary aftershock zone.

## DISCUSSION

For the 2011 Mineral, VA aftershock zone the moment tensor inversion method of Ebel and Bonjer (1990) and relative location method of Ebel et al. (2008) define a complicated set of fault structures that consist of two primary planes (Q1 and Q2), one smaller planar feature (Q3), along with some off-fault seismicity near the intersection of planes Q1 and Q2 (Figures 17 and 22). Planes Q1, Q2, and Q3 are all part of the Quail fault zone named by Horton et al. (2012a, 2012b) (Figure 9). The seismicity of the northernmost primary fault plane (Q1) has a strike and dip of  $045^{\circ}/67^{\circ}$ , whereas Q2 has a strike and dip of  $002^{\circ}/72^{\circ}$ . Q3 has a strike and dip of  $056^{\circ}/58^{\circ}$ , striking northeast similar to Q1 but with a shallower dipping plane.

Results of the moment tensor inversion for events on the southern primary fault plane (Q2) show focal mechanisms with one of their nodal planes with similar strikes and dips to the trend in seismicity as imaged in the relative location analysis (Figure 20). Focal mechanisms calculated for events on Q1 also have one set of nodal planes similar to the strike and dip of the local trend in the seismicity as determined by the relative location analysis (Figure 21). Fault motion on Q1 and Q2 is primarily pure thrust with a few instances of normal faulting (Figures 20 and 21).

The shallow cluster of events offset about 1-2 km to the northwest of the main fault illuminate a small planar fracture with strike and dip that is similar to the main fault, but this northwestern seismicity cluster seems to have experienced normal fault motion in the month following the mainshock (Figure 21). This normal fault motion, somewhat offset from the main fault structure, could be due to brittle rupture of a region in the

mainshock footwall that experienced tensional stresses following the main thrust event (Lin and Stein, 2004; Figure 23).

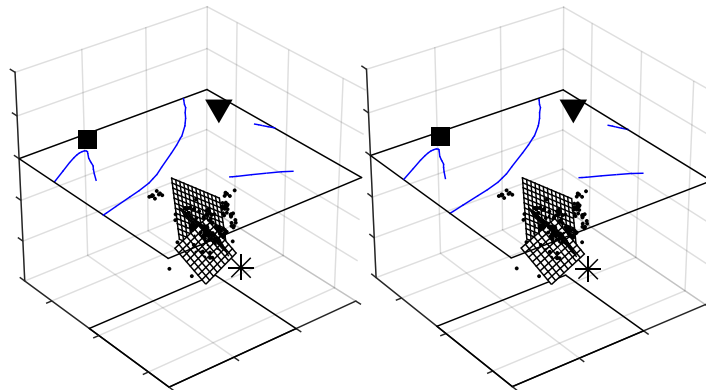
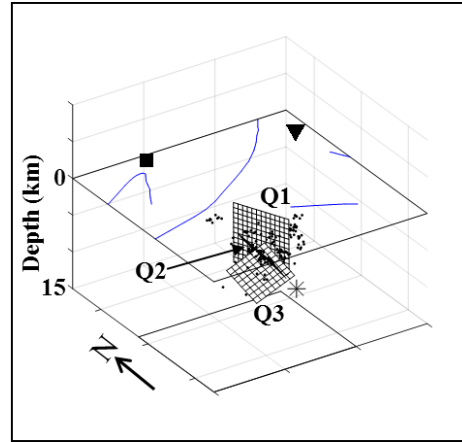


**Figure 22.** Oblique stereo pair shows the three intersecting gridded planes (Q1, Q2, and Q3) that are part of the Quail Fault of Horton et al. (2012a; 2012b). Plane Q2 intersects both planes Q1 and Q3 and is difficult to see from this view. The Mw 5.8 main event hypocenter is represented by the asterisk, and the surface locations of known faults in the area as of 1993 are shown as blue lines. The black square is the town of Louisa and the black triangle is the town of Mineral. Black dots are relative location hypocenters with a location uncertainty of one standard deviation ( $\sigma$ ) < 0.1 km. The boxed figure above the stereo pair labels the fault planes shown in the stereo view images.

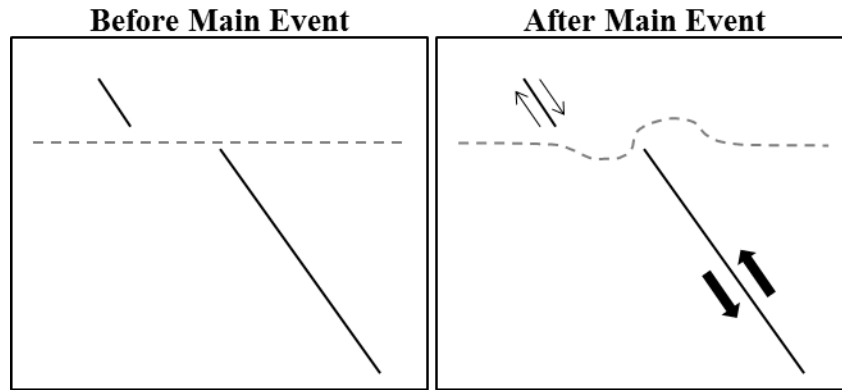


**Figure 23.** A simplified cross-section of the subsurface looking northeast along strike of the main fault. The small shallow seismic structure slightly offset from the main fault is also shown. The dashed line represents a horizontal surface before the 2011 main event that experienced tensile stress in the footwall block just above the shallow tip of the rupture and compressional stress in the hanging wall block just above the shallow tip of the rupture following reverse fault motion. Normal faulting apparently occurred on the shallow offset structure in response to the tensile stress generated by the displacement associated with the mainshock rupture.

Relative location hypocenters of the aftershocks several kilometers to the northeast of the main fault depict a steeply dipping planar feature with a strike and dip of  $033^{\circ}/85^{\circ}$ , and this structure has been given the name Fredericks Hall Fault by Horton et al. (2012a, 2012b) (Figure 9). The radiation patterns of the body waves could not be constrained by the moment-tensor inversion method for events associated with the Fredericks Hall Fault due to the lack of stations east and north of the hypocenters. The locations of the small cluster of events between the main fault aftershock zone and the Fredericks Hall Fault show little in the way of a consistent trend in strike or dip of a planar feature. For mainshocks at other continental locations outside of the CVSZ, distributed aftershock zones and abundant off-fault seismicity similar to the events northeast of the main fault and the shallow offset cluster of events to the northwest following the 2011 main event in Virginia have been observed for blind thrust rupture events (Lin and Stein, 2004). Thus, the off-fault clusters of aftershocks in Virginia

following the 2011 earthquake are probably not unusual for the aftershocks of intraplate earthquakes in continental settings.

Analysis of the temporal evolution of the 2011 Virginia aftershock sequence reveals that during the first week following the Mw 5.8 main event seismicity occurred at all locations along strike and dip on the main fault, along the Fredericks Hall Fault, and in the small cluster of events between the mainshock rupture zone and the Fredericks Hall Fault (Figures 24 and 25). A concentration of events occurred between 8/28-8/30 in the footwall near the intersection of the two main fault planes, with shallow seismicity occurring along the southwestern fault plane from 8/29-8/31 (Figure 24). The Fredericks Hall Fault and the cluster of events slightly west of this fault experienced seismicity in the last week of August. The Fredericks Hall Fault events appear to have spread north from 37.97° N and south from 37.98° N to meet around 37.975° N from 08/25-09/30 (Figures 24 and 25). The shallow cluster of events slightly northwest of the main fault appears to originate at a depth of 3 km and propagate up-dip to shallower depths of 1.5-2 km from 8/30 to 9/20 (Figure 24). The events that were characterized by normal faulting on the shallow seismic structure offset to the northwest from the main fault occurred from about 15 to 30 days following the mainshock. The frequency of seismicity decreased for the months of October, November, and December 2011 and is localized near the intersection of the primary fault planes Q1 and Q2 at 37.94° N during this time frame (Figure 24). The shallow seismic structure slightly northwest of the main fault experienced an increase in seismic activity throughout December after two months of few to no aftershocks (Figure 24). There were clearly migrations of post-mainshock

deformations during the several months following the 2011 main event, as indicated in Figure 24.

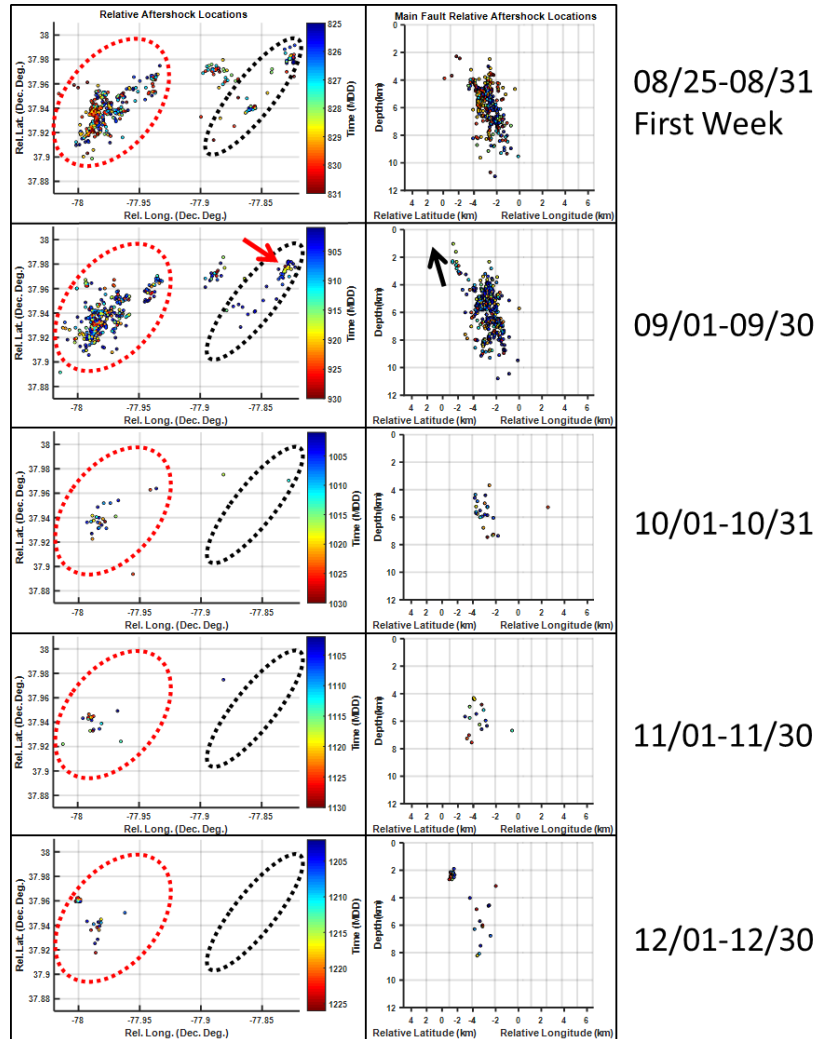


**Figure 24.** Relative location hypocenters colored by event origin time. The left column is a map view of all relative aftershock locations and the right column is a cross sectional view of the main fault looking into the paper at an azimuth of 034°N, approximately along strike of the main fault. The location of the main fault is shown by the red dashed ellipse and the location of Fredericks Hall Fault is shown by the black dashed ellipse. The propagation of events in the northeast portion of Fredericks Hall Fault from 37.97° N and south from 37.98° N to meet around 37.975° N during September is shown by the red arrow in the left column. The black arrow in the right column shows the direction of propagation of aftershocks in the shallow cluster of events slightly west of the main fault. These latter events originate at a depth of 3 km and propagate up-dip to shallower depths of 1.5-2 km from 8/30 to 9/20.

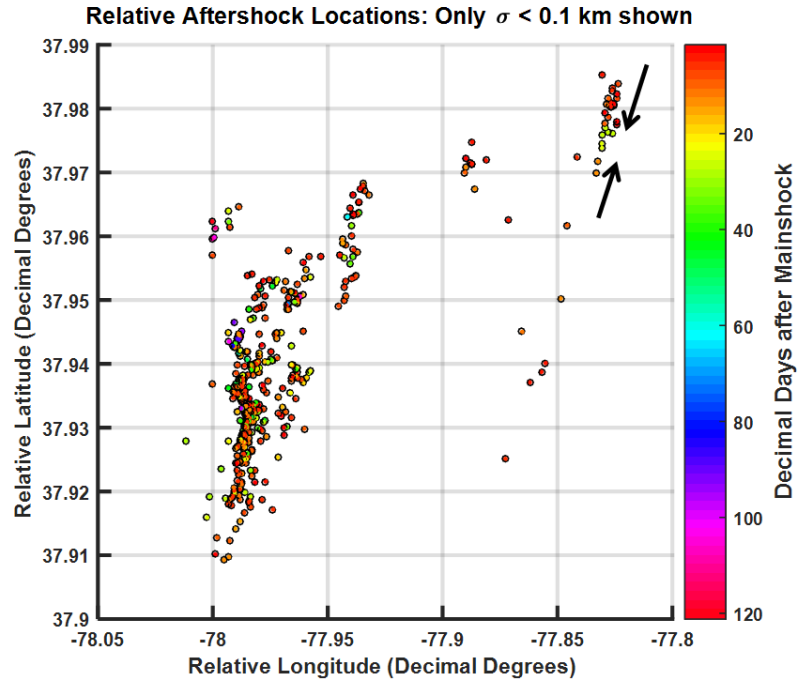


**Figure 25.** Map view relative locations with standard deviation ( $\sigma$ )  $< 0.1$  km colored by progressing time following the Mw 5.8 main event. The color bar is labeled by decimal days following the mainshock. Seismicity progressing from north to south and south to north to meet in the middle at 37.975 °N on the Fredericks Hall Fault is shown by the two black arrows. The majority of events occur in the first twenty days following the main event.

The location of the Mineral, VA earthquake within the CVSZ may have resulted from the combination of the east-west to southeast-northwest direction of maximum compressive stress (Kim and Chapman, 2005; Herrmann, 2011; Chapman, 2013; McNamara et al., 2014a) and the northeast striking geophysical anomalies near the epicentral area (Horton et al., 2015b; Shah et al., 2015). The increase in the shear stress-to-normal stress ratio due to the bend in strike of the geologic units near the main event and the southeast-northwest orientation of maximum compressive stress near the mainshock epicenter likely controlled the location of fault slip (Shah et al., 2015). Focal mechanisms calculated for aftershocks in this study depict thrust motion with P axes ranging from east-west to southeast-northwest, indicating a direction of average maximum compressive stress similar to that found in previous studies (Kim and

Chapman, 2005; Herrmann, 2011; Chapman, 2013; McNamara et al., 2014a; Figures 20 and 21).

The rocks of the CVSZ have experienced multiple metamorphic and tectonic events during their geological history, which resulted in foliations, structural fabric, faults, and dikes that all contribute to preexisting orientations of structures in the epicentral region (Burton et al., 2014; Burton et al., 2015; Horton et al., 2015a; Hughes et al., 2015; Pratt et al., 2015; Shah et al., 2015). North to northeast striking foliations and joints have been found at the surface (Burton et al., 2014; Burton et al., 2015; Hughes et al., 2015) and preexisting faults have been identified in the subsurface (Coruh et al., 1988; Pratt et al., 2015). Dips of faults observed on the I-64 seismic profile are shallower than the dips determined for the Quail fault structure, indicating that the Quail Fault does not extend as far south as I-64 on a structure with visible offset on the seismic profile (Pratt et al., 2015). Rock outcrops between the surface projection of the Quail Fault and the southern extension of the Long Branch Fault have structural fabrics that are indicative of a past high-strain environment, and this area has been labeled the Bend of River high-strain zone (Hughes et al., 2015; Figures 9 and 10). Two distinct planar foliation orientations have been determined in this area with strikes and dips of  $037^{\circ}/42^{\circ}$  and  $001^{\circ}/25^{\circ}$ . The former has been observed to be parallel to the east and southeast-dipping, compositionally variable layers and discontinuous lenses comprising the Chopawamsic Formation (Hughes et al., 2015). The strikes of these foliations are similar to the strikes determined in this study for the two primary fault planes Q1 and Q2. Joints in the Chopawamsic Formation overlying the epicentral area have been found to strongly trend  $N15^{\circ}E$  and  $N50^{\circ}E$  to  $N60^{\circ}E$  and to dip southeast (Burton et al., 2015). Although no

evidence of shear slip along these joints has been identified, some evidence of small-scale slip has been observed on numerous foliation-joint planes with similar strikes and dips as the two primary planes of the Quail Fault structure determined in this study (Burton et al., 2015). It is likely that the geometry of the faulting on the Quail Fault was controlled by a preexisting structural fabric that was activated during the 2011 Mineral, VA mainshock.

## CONCLUSION

The relative location method used in this study defined a complicated fault structure that was illuminated by the aftershock sequence following the 2011 main event. The structure is comprised of three fault planes, two primary planes and one smaller plane with strikes and dips of  $045^{\circ}/67^{\circ}$ ,  $002^{\circ}/72^{\circ}$ , and  $056^{\circ}/58^{\circ}$ , respectively. The moment tensor inversion method used in this study produced focal mechanisms that had nodal planes with similar strikes and dips as the trends delineated by the seismicity. The majority of the focal mechanisms depicted thrust faulting with a few instances of normal faulting on the main fault structure and on the shallow offset structure slightly northwest of the main fault structure.

Seismicity occurred during the first week following the main event at all locations on the main fault structure, on the Frederick's Hall Fault, and the small cluster of events between the mainshock rupture zone and the Frederick's Hall Fault. Aftershocks later became concentrated at the fault plane intersections on the main fault structure and migrated to shallower depths on the main fault structure, Frederick's Hall Fault, and the small cluster of events between the mainshock rupture zone and the Frederick's Hall Fault in the weeks following the main event. Normal faulting in the shallow cluster of events

slightly northwest of the main fault occurred from 15-30 days following the mainshock, which was then followed by a decrease in seismic activity and a resurgence of seismicity 4 months after the main event.

Trends in the structural fabric of the bedrock in the epicentral area have similar strikes and dips as those calculated for the two primary fault planes and the smaller fault plane on the main fault structure. Pre-existing structural fabric within the bedrock of the CVSZ likely controlled the geometry of the multi-planar Quail Fault structure that was activated during the 2011 Mineral, VA mainshock. These pre-existing weaknesses in the crystalline bedrock of the CVSZ likely control the location of stress concentration and inherent location of the initiation of fault rupture in seismic events such as the 23 August 2011 Mineral, Virginia, earthquake.

Results of this study illustrate an example of the type of complicated fault structure that is activated during seismic events in the CVSZ and perhaps at other intraplate settings and shows the migration of post-main event seismic activity on such a structure. Rapid deployment of dense seismometer networks and in-depth analyses of the recorded aftershock sequences following main shocks as exemplified in this study are crucial for the progression of the scientific understanding of the infrequent, yet damaging, intraplate earthquakes.

## REFERENCES

- Bailey, C.M., 1999a, William & Mary, <http://web.wm.edu/geology/virginia/provinces/terrane.html>, Web, Nov. 2013.
- Bollinger, G.A., 1973a, Seismicity and crustal uplift in the southeastern United States, *American Journal of Science*, v. 273A, p 396-408.
- Bollinger, G.A., 1973b, Seismicity of the southeastern United States, *Bulletin of the Seismological Society of America*, v. 63, p. 1785-1808.
- Bollinger, G.A., Chapman, M.C., and Moore, T.P., 1980, Central Virginia regional seismic network: Crustal structure in central and southwestern Virginia, NUREG/CR-1217, U.S. Nuclear Regulatory Commission, Washington, D.C., 187 p.
- Bollinger, G.A. and Hopper, M.G., 1972, The earthquake history of Virginia-1900-1970, Virginia Polytechnic Institute and State University, Research Division.
- Bollinger, G.A. and Sibol, M.S., 1985, Seismicity, seismic reflection studies, gravity and geology of the central Virginia seismic zone: Part I. Seismicity, *Geological Society of America Bulletin*, v. 96, p. 49-57.
- Burton, W.C., Spears, D.B., Harrison, R.W., Evans, N.H., Schindler, J.S., and Counts, R., 2014, Geology and neotectonism in the epicentral area of the 2011 M5.8 Mineral, Virginia, earthquake, *in* Baily, C.M. and Coiner, L.V., eds., *Elevating Geoscience in the Southeastern United States: New Ideas about Old Terranes: Field Guides for the GSA Southeastern Section Meeting*, Blacksburg, Virginia, 2014: Geological Society of America Field Guide 35, p. 103-127.
- Burton, W.C., Harrison, R.W., Spears, D.B., Evans, N.H., and Mahan, S., 2015, Geologic framework and evidence for neotectonism in the epicentral area of the 2011 Mineral, Virginia, earthquake, *in* Horton, J.W., Jr., Chapman, M.C., and Green, R.A., eds., *The 2011 Mineral, Virginia, Earthquake, and Its Significance for Seismic Hazards in Eastern North America: Geological Society of America Special Paper 509*, p. 345-376.
- Chapman, M.C., 2013, On the Rupture Process of the 23 August 2011 Virginia Earthquake: *Bulletin of the Seismological Society of America*, v. 103, no. 2A, p. 613-628.
- Coruh, C., Bollinger, G.A., and Costain, J.K., 1988, Seismogenic structures in the central Virginia seismic zone: *Geology*, v. 16, p. 748-751.

- Dicken, C. L., Nicholson, S. W., Horton, J. D., Kinney, S. A., Gunther, G., Foose, M. P., and Mueller, J. A. L., 2005, Integrated Geologic Map Databases for the United States: Delaware, Maryland, New York, Pennsylvania, and Virginia: U.S. Geological Survey Open-File Report 2005-1325, U.S. Geological Survey, Reston, VA.
- Ebel, J.E. and Bonjer, K.-P., 1990, Moment tensor inversion of small earthquakes in southwestern Germany for the fault plane solution: *Geophysical Journal International*, v. 101, p. 133-146.
- Ebel, J.E., Moulis, A.M., Smith, D., and Hagerty, M., 2008, The 2006-2007 Earthquake Sequence at Bar Harbor, Maine: *Seismological Research Letters*, v. 79, no. 3, p. 457-468.
- Faill, R.T., 1998, A geologic history of the North-Central Appalachians, part 3. The Alleghany Orogeny, *American Journal of Science*, v. 298, p. 131-179.
- James, D.E., Smith, T.J., and Steinhart, J.S., 1968, Crustal structure of the middle Atlantic states, *Journal of Geophysical Research*, v. 73, no. 6, p. 1983-2007.
- Herrmann, R.B., 2011, St. Louis University Earthquake Center website, [http://www.eas.slu.edu/eqc/eqc\\_mt/MECH.NA/20110823175105/index.html](http://www.eas.slu.edu/eqc/eqc_mt/MECH.NA/20110823175105/index.html), Web, Nov. 2014.
- Hopper, M.G. and Bollinger, G.A, 1971, The earthquake history of Virginia-1774-1900, Virginia Polytechnic Institute and State University, Research Division.
- Horton, J.W., Jr., Chapman, M.C., Carter, A.M., Carter, M.W, Harrison, R.W., Herrmann, R.B., and Snyder, S.L., 2012a, Faults delineated by aftershocks associated with the 2011 central Virginia earthquake and their tectonic setting: *Geological Society of America Abstracts with Programs*, v. 44, no. 4, p. 14.
- Horton, J.W., Jr., McNamara, D.E., Shah, A.K., Gilmer, A.K., Carter, A.M., Burton, W.C., Harrison, R.W., Carter, M.W., Herrmann, R.B., and Snyder, S.L., 2012b, Preliminary analysis of magnitude 5.8 Virginia earthquake causative fault and subsidiary faults illuminated by aftershocks: *Geological Society of America Abstracts with Programs*, v. 44, no. 7, p. 381.
- Horton, J.W., Jr., Chapman, M.C., and Green, R.A., 2015a, The 2011 Mineral Virginia, earthquake, and its significance for seismic hazards in eastern North America- Overview and synthesis, *in* Horton, J.W., Jr., Chapman, M.C., and Green, R.A., eds., *The 2011 Mineral, Virginia, Earthquake, and Its Significance for Seismic Hazards in Eastern North America: Geological Society of America Special Paper 509*, p. 1-25.

- Horton, J.W., Jr., Shah, A.K., McNamara, D.E., Snyder, S.L., and Carter, A.M., 2015b, Aftershocks illuminate the 2011 Mineral, Virginia, earthquake causative fault zone and nearby active faults, *in* Horton, J.W., Jr., Chapman, M.C., and Green, R.A., eds., *The 2011 Mineral, Virginia, Earthquake, and Its Significance for Seismic Hazards in Eastern North America: Geological Society of America Special Paper 509*, p. 253-271.
- Hughes, K.S., Hibbard, J.P., and Bohnenstiehl, D.R., 2015, Relict Paleozoic faults in the epicentral area of the 23 August 2011 central Virginia earthquake: Assessing the relationship between preexisting strain and modern seismicity, *in* Horton, J.W., Jr., Chapman, M.C., and Green, R.A., eds., *The 2011 Mineral, Virginia, Earthquake, and Its Significance for Seismic Hazards in Eastern North America: Geological Society of America Special Paper 509*, p. 331-343.
- Kim, W.-Y., and Chapman, M., 2005, The 9 December 2003 Central Virginia Earthquake Sequence: A Compound Earthquake in the Central Virginia Seismic Zone: *Bulletin of the Seismological Society of America*, v. 95, no. 6, p. 2428-2445.
- Lin, J., and Stein, R.S., 2004, Stress triggering in thrust and subduction earthquakes and stress interaction between the southern San Andreas and nearby thrust and strike-slip faults: *Journal of Geophysical Research*, v. 109, B02303, p. 1-19.
- McNamara, D.E., Benz, H.M., Herrmann, R.B., Bergman, E.A., Earle, P., Meltzer, A., Withers, M., and Chapman, M., 2014a, The Mw 5.8 Central Virginia seismic zone earthquake sequence of August 23, 2011: Constraints on earthquake source parameters and fault geometry: *Bulletin of the Seismological Society of America*, v. 104, p. 40-54.
- McNamara, D.E., Gee, L., Benz, H.M., and Chapman, M., 2014b, Frequency-dependent seismic attenuation in the Eastern United States as observed from the 2011 Central Virginia earthquake and aftershock sequence, *Bulletin of the Seismological Society of America*, v. 104, no. 1, p. 55-72.
- Pratt, T.L., Coruh, C., Costain, J.K., and Glover, L. III, 1988. A geophysical study of the earth's crust in central Virginia: Implications for Appalachian crustal structure, *Journal of Geophysical Research*, v. 93, no. B6, p. 6649-6667.
- Pratt, T.L., Horton, J.W., Jr., Spears, D.B., Gilmer, A.K., and McNamara, D.E., 2015, The 2011 Virginia Mw 5.8 earthquake: Insights from seismic reflection imaging into the influence of older structures on eastern U.S. seismicity, *in* Horton, J.W., Jr., Chapman, M.C., and Green, R.A., eds., *The 2011 Mineral, Virginia, Earthquake, and Its Significance for Seismic Hazards in Eastern North America: Geological Society of America Special Paper 509*, p. 285-294.
- Scherbaum, F., 1996, *Of Poles and Zeros: Dordrecht, The Netherlands, Kluwer Academic Publishers*, 272 p.
- Scherbaum, F., and Bouin, M. -P., FIR filter effects and nucleation phases: *Geophysical Journal International*, v. 130, p. 661-668.

- Shah, A.K., Horton, J.W., Jr., Burton, W.C., Spears, D.B., and Gilmer, A.K., 2015, Subsurface geologic features of the 2011 central Virginia earthquakes revealed by airborne geophysics, *in* Horton, J.W., Jr., Chapman, M.C., and Green, R.A., eds., The 2011 Mineral, Virginia, Earthquake, and Its Significance for Seismic Hazards in Eastern North America: Geological Society of America Special Paper 509, p. 295-304.
- Stein, S., Cloetingh, S., Sleep, N., and Wortel, R., 1989, Passive margin earthquakes, stresses, and rheology, *in* Gregersen, S., and Basham, P., eds., Earthquakes at North-Atlantic passive margins: Dordrecht, The Netherlands, Kluwer Academic Publishers.
- Waldhauser, F. and Ellsworth, W.L., 2000, A Double-Difference Earthquake Location Algorithm: Method and Application to the Northern Hayward Fault, California: Bulletin of the Seismological Society of America, v. 90, no. 6, p. 1353-1368.
- Withjack, M.O., Schlische, R.W., and Olsen, P.E., 1998, Diachronous rifting, drifting, and inversion on the passive margin of central eastern North America; and analog for other passive margins, American Association of Petroleum Geologists Bulletin, v. 82, no. 5A, p. 817-835.
- Wolin, E., Stein, S., Pazzaglia, F., Meltzer, A., Kafka, A., and Berti, C., 2012, Mineral, Virginia, earthquake illustrates seismicity of a passive-aggressive margin, Geophysical Research Letters, v. 39. p. 1-7.
- Zoback, M.L. and Zoback, M.D., 1989, Tectonic stress field of the continental United States, *in* Parkiser, L.C. and Mooney, W.D., eds., Geophysical framework of the continental United States: Geological Society of America Memoir, v. 172, p. 523-539.